DEVELOPMENT AND EVALUATION OF INCOHERENT SCATTERING SPECTROSCOPY FOR SPATIAL AND SPECTRAL CHARACTERIZATION OF HIGH-ENERGY X-RAY BEAMS

By

TEXIN LI

A DISSERTATION PRESENTED TO THE GRADUATE SCHOOL OF THE
UNIVERSITY OF FLORIDA IN PARTIAL FULFILLMENT OF THE
REQUIREMENTS FOR THE DEGREE OF
DOCTOR OF PHILOSOPHY

UNIVERSITY OF FLORIDA

2000

ACKNOWLEDGMENTS

The author is very grateful to all the people whose contributions have made this research project successful.

Special thanks go to Dr. Samim Anghaie for his constant financial support and valuable suggestions that helped to guide the direction of this project. Dr. Travis Knight, Mr. Ward Dougherty, Dr. Gary Chen, Mrs. Sarah White, and especially Dr. Morgan White helped in simulation. The author is greatly indebted to Dr. Angelo Ferrari for his superb experimental skills. Dr. Wolfgang Tome, Dr. Siyong Kim, and Mr. Joon Ho Park also helped in the experiment work. Dr. Chihray Liu provided the relevant references and pertinent comments. Dr. Wesley Bolch was kind enough to permit the author to run codes at his workstations and Mr. Didier Rajon helped in setting up the account.

The author would also like to take this chance to express his sincere gratitude to other classmates and faculty members at the Nuclear and Radiological Engineering Department and the Radiation Oncology Department for their constructive suggestions and their helpful comments.

The author thanks Dr. Iain C. Trevena, Mr. Colette Pigeon-Jolicoeur, and Mr. Dave Willinson at MDS Nordion for providing the necessary data needed for the MCNP simulation.

TABLE OF CONTENTS

page

ACKNOWLEDGMENTS.....ii

LIST OF TABLES.....v

LIST OF FIGURES.....vi

ABSTRACT.....ix

CHAPTERS

1 INTRODUCTION.....1

2 THEORY OF INCOHERENT SCATTERING METHOD.....18

Scattering.....18
Coherent Scattering.....19
Incoherent Scattering.....21
Choice of Scattering Angle.....24
Effect of Collimator.....26
Choice of Shielding Materials.....32
Choice of Scattering Materials.....33
Detector Response.....37

3 MATERIALS AND METHODS.....41

Cobalt-60 Therapy Machine.....41
High Purity Germanium Detector.....44
Electronics.....45
Experimental Setup.....47
Measurement of Spectra.....48 +
Effect of Collimator.....49 +

4 RESULTS AND DISCUSSION.....50

Scattered Spectra.....50
Effect of Collimator.....55

5 MONTE CARLO SIMULATION..60

Scattered Spectrum of Cobalt-60 Beam Simulation 62
Modeling of Cobalt-60 Machine..64
Primary Spectrum Simulation of Cobalt-60 Machine.............................66
Scattered Spectrum Simulation of Cobalt-60 Machine 67
Effect of the Collimator..69

6 APPLICATION TO MEDICAL LINEAR ACCELERATOR..........................76

Description of Medical Linear Accelerator..76
Measurement of Spectrum...80
Monte Carlo Simulation..84

7 CONCLUSIONS..91

APPENDICES

A MCNP INPUT FILE FOR COBALT-60 MACHINE SIMULATION...........95

B MCNP INPUT FILE FOR SL25 LINAC SIMULATION.........................100

REFERENCES CITED...111

BIOGRAPHICAL SKETCH...115

LIST OF TABLES

Table page

2-1. Minimum scattering angles (in degree)……………………………………26

2-2. The geometric line broadening (in keV) of 100 keV Photons………………..28

2-3. The geometric line broadening (in keV) of 1000 keV Photons………………29

2-4. The geometric line broadening (in keV) of 10 MeV Photons………………...30

6-1. Peaks observed in neutron irradiated HPGe detector………………………...82

LIST OF FIGURES

Figure page

2-1. Atomic form factor versus momentum transfer parameter for elements carbon and lead (normalized to Z^2)..20

2-2. Incoherent scattering functions versus momentum transfer parameter for elements carbon and lead (normalized to Z)....................................23

2-3. Optimal scattering angle for different detecting ranges and incident photon energy..27

2-4. Geometric line broadening for 100 keV photons....................................29

2-5. Geometric line broadening for 1000 keV photons...................................30

2-6. Geometric line broadening for 10 MeV photons.....................................31

2-7. The Photon Cross Sections for Lead..32

2-8. Differential atomic coherent and incoherent cross sections for 100 keV photons in carbon..34

2-9. Differential atomic coherent and incoherent cross sections for 1250 keV photons in carbon..35

2-10. Differential atomic coherent and incoherent cross sections for 5000 keV photons in carbon..35

2-11. Differential atomic coherent and incoherent cross sections for 100 keV photons in lead..36

2-12. Differential atomic coherent and incoherent cross sections for 1250 keV photons in lead..36

2-13. Differential atomic coherent and incoherent cross sections for 5000 keV photons in lead..37

3-1. A schematic electronic system for gamma spectroscopy……..…………………45

3-2. The Experimental setup of incoherent scattering method (not to scale) ……....47

4-1. Measured scattered spectrum from cobalt-60 machine……...………………....51

4-2. The reconstructed spectrum from the measured scattered spectrum (only two peaks) are shown……...………………………………….……………..52

4-3. Primary photon peaks from cobalt-60……..……..……………………………53

4-4. Cobalt-60 spectrum with lead shielding……..………………………………...55

4-5. Cobalt-60 spectrum without lead shielding…………………………...………..56

4-6. Cesium-137 spectrum with lead shielding……………………………..…...……..57

4-7. Cesium-137 spectrum without lead shielding……………………….…...……..58

5-1. MCNP simulation geometry for point beam and size beam………..…...……..62

5-2. Simulated spectrum from cobalt-60 point source with 90° scattering (point beam case) ……...……………………………………………………63

5-3. Simulated spectrum from cobalt-60 machine with 90° scattering (size beam case) ……………………………………………..…..……..64

5-4. Source design of Theratron 1000 cobalt-60 therapy machine……...…………65

5-5. Simulated primary spectrum form cobalt-60 machine…………………...……..66

5-6. The actual MCNP geometry of the cobalt-60 machine head and the measurement setup……………………………………………………68

5-7. The actual simulation of the cobalt-60 machine with 90° scattering…………....68

5-8. MNCP simulated spectra from cobalt -60 with 5.0 cm thick copper collimator, r is the radius of the pinhole of the collimator…………………....70

5-9. Simulated spectra from cobalt-60 with 5.0 cm thick lead collimator, r is the radius of the pinhole of the collimator……………………………....71

5-10. Photon cross sections for copper in the energy range of 10 keV-MeV……….72

5-11. Photon cross section for lead in the energy range of 10 keV-2 MeV………....73

5-12. Simulate spectrum from cobalt-60 with 20.0 cm lead collimator, r=0.6 cm.....74

6-1. Photoneutron production cross sections for tungsten..............................80

6-2. Photonneutron production cross sections in lead....................................81

6-3. Neutron induced spectral characteristics of HPGe detector in the maze of a radiation therapy room with a linear accelerator operating at 20 MV..........83

6-4 . Geometry of MCNP simulation of SL25 Linac.......................................85

6-5. MCNP simulated primary flux spectra through the scatter surface and in the scatter...86

6-6. Comparison of theoretically predicted scattered flux spectrum from primary flux in the scatterer and MCNP simulated scattered flux spectrum....................87

6-7. Comparison of reconstructed primary flux spectrum and MCNP simulated primary flux spectrum...88

6-8. Measurement resolution versus reconstructed resolution with 90° scattering by different incident energy..89

6-9. Measurement resolution versus reconstructed resolution for incident energy of 20 MeV with different scattering angles.............................90

Abstract of Dissertation Presented to the Graduate School of the
University of Florida in Partial Fulfillment of the
Requirements for the Degree of Doctor of Philosophy

DEVELOPMENT AND EVALUATION OF INCOHERENT SCATTERING SPECTROSCOPY FOR SPATIAL AND SPECTRAL CHARACTERIZATION OF HIGH-ENERGY X-RAY BEAMS

By

Texin Li

December, 2000

Chairman: Samim Anghaie
Major Department: Nuclear and Radiological Engineering

While the knowledge about the spectral information from high energy x-ray machines is fundamental in some applications, like megavoltage photon therapy, how to get the information presents a daunting task. The difficulty lies in the fact that the detector is always inundated with billions of particles, and will be saturated instantly. In addition, the detecting efficiency falls off drastically at high energy. To remedy this situation, the scattering method is proposed and has been tried on several occasions. The scattering method can effectively reduce the high intensity and the energy spectrum is shifted to a suitable range. However, in applying this method to a practical situation, attention should be paid to some complicating factors.

In this research project, a complete formulation for the incoherent scattering method is given; the scattering method is then applied to a cobalt-60 radiation therapy machine, and the scattered spectrum is measured and then transformed back to the primary spectrum. When the Monte Carlo technique (MCNP) is used to simulate the scattered spectrum, good agreement is observed. The broadening effect inherent to the scattering method is introduced and demonstrated quantitatively for the first time. The broadening effect is the cause of energy resolution loss when the measured scattered spectrum is transformed back to the incident spectrum. Also, the effect of the collimator is observed experimentally and Monte Carlo (MCNP) simulation confirms the observation. Methods are proposed to minimize this unwanted complication based on the radiological properties of materials and the physical design of the collimator.

The incoherent scattering method has been applied to medical electron accelerators using the Monte Carlo (MCNP) technique. The primary and the scattered spectra are obtained under ideal experimental conditions. The MCNP simulated scattered spectrum is transformed back to primary spectrum and good agreement is observed.

CHAPTER 1
INTRODUCTION

The spectral distribution of high-energy x-ray beams is a fundamental quantity from which, in principle, all required information relevant to the function of x-ray machines can be determined. In diagnostic radiology, the spectrum is important to determine the patient dose and the image quality. In radiation therapy, the spectrum can provide the fullest description of a beam's quality and may be used for dose calculation using convolution techniques (Boyer and Mok 1985, Ahnesjo et al. 1987, Mackie et al. 1988, Zhu and Boyer 1990). It also allows accurate calculation of stopping power ratios for improved dosimetry at high photon energies and, if measured on a regular basis, provides routine quality assurance protocols with a quantitative measure of any changes in spectral output.

It is also important to know the variation of energy spectrum as a function of radial distance from the central ray. The bremsstrahlung energy spectrum in the central part of a photon beam is somewhat harder than in the region near the edge of the beam. The flattening filter not only hardens the beam as a whole, but further enhances the relative hardness near the center as well. Consequently, the relative depth dose in tissue will vary as a function of distance from the central ray of the beam.

The ideal solution would be to measure the spectrum and angular distributions with either a NaI(Tl) scintillator, a germanium detector, or by some other means. Unfortunately, such spectrometry of high energy x-rays is hardly suited for this purpose for two reasons. First the high intensity radiation from a medical linear accelerator excludes any possibility of measuring the spectrum directly. The typical photon fluence rate encountered in radiography may be as large as 10^8 photons cm^{-2} sec^{-1} at a 100 cm distance between the focal spot and the detector under exposure conditions of 100 kV and 15 mA (Birch et al. 1979). In a radiation therapy environment, for a linear accelerator operating at a nominal 6 MV (with a dose rate of 400 centi-grays per minute at a distance of 100 cm, average beam current of about 100 microamperes, pulse repetition frequency of 300 pulses per second, and a pulse duration of 3.5 microseconds), the photon flux at the isocenter is very high, on the order of 10^{10} photons cm^{-2} sec^{-1} at 100 cm. Currently, semiconductor spectrometers can only analyze photon count rates up to 10^5 to 10^6 photons per second. Secondly, the detecting efficiency of the current detectors falls off as the energy of the x-rays goes up. At energies above several MeVs, the absolute efficiency is close to zero.

To circumvent these difficulties, a number of methods have been tried to get the spectral information from x-ray machines, including medical electron accelerators. One of them is the transmission method. The measurement of a transmission curve is relatively simple to carry out to a high degree of accuracy. In this method, the dose transmission curve is measured using ion chambers. From this curve, the original energy spectra can be reconstructed using an iterative least-square technique and Laplace transform pairs. When the detector is placed in a beam of x-rays, the photon fluence, Φ, causes a detector signal, S. The energy spectrum of the fluence is $\Phi_E = d\Phi/dE$, and

$$S = \int_0^\infty \Phi_E R(E) dE, \tag{1-1}$$

where R(E) is the signal produced by unit fluence of photon energy, E. If an attenuator of thickness x is placed in a well-collimated beam, the energy spectrum of the fluence changes to,

$$\Phi_E(x) = \Phi_E(0) e^{-\mu x}, \tag{1-2}$$

where μ is the attenuation coefficient for photons of energy, E, and the signal, S, becomes a function of x:

$$S(x) = \int_0^\infty \Phi_E(0) e^{-\mu x} R(E) dE. \tag{1-3}$$

The relative transmission, T(x), measured is the ratio between the signals with an attenuator of thickness x and without attenuator:

$$T(x) = S(x)/S(0). \tag{1-4}$$

By introducing

$$F(E) = \Phi_E(0)R(E)/S(0), \tag{1-5}$$

the transmission ratio can be written as,

$$T(x) = \int_0^\infty F(E)e^{-\mu x}dE. \tag{1-6}$$

The function F(E) is defined such that F(E)dE expresses the fraction of the total signal that is due to photons of energy between E and (E+dE) in the unattenuated beam. By changing variables from energy, E, to attenuation coefficient, μ, Eq. (1-6) can be rewritten

$$T(x) = \int_0^\infty f(\mu)e^{-\mu x}d\mu, \tag{1-7}$$

where

$$f(\mu) = -F(E)dE/d\mu. \tag{1-8}$$

Thus, f(μ) is the fraction of the total signal produced by photons with attenuation coefficient μ per dμ interval in the unattenuated beam. It is assumed that μ(E) decreases monotonically from $\mu(0)=\infty$ to $\mu(\infty)=0$.

Eq. (1-7) is a Laplace transformation of the function f(μ). The relative transmission can be represented by different expressions by choosing different curve-fitting parameters, and the inverse Laplace transformation of the T(x) gives the f(μ).

Several successful reconstruction models have been developed in the diagnostic and low-megavoltage energy region (Archer and Wagner 1982, Archer et al. 1985, Huang et al. 1982, Ahuja et al. 1986, Dance 1987). At these energies the total attenuation coefficient is steeply decreasing and, therefore, provides good differentiation between successive energy intervals. A complicating factor in the megavoltage region, however, is the reduction in energy differentiation due to the slowly decreasing Compton cross-section and increased contribution of the pair production cross-section to the total attenuation coefficient, making the task of deriving spectra more demanding on the method employed. Despite this fact, several reconstruction models for use in the megavoltage region have appeared in the literature using iterative approaches and by considering the production of bremsstrahlung through a thick transmission target (Ahnesjo and Andreo 1989, Huang et al. 1982, 1983, Piermattei et al. 1990, Sauer and Neumann 1990). The amount of spectral information obtainable by this method is limited by the accuracy to which the transmission curve can be measured and by the limited number of parameters used in the curve fitting. In general, the principle of attenuation analysis has been to fit the attenuation curve with an analytical function containing two or more parameters. The inverse Laplace transformation of this attenuation curve is then formulated and contains these parameters. The transmission method is not a method comparable to spectrometry in the fine-structure of the resulting distribution that can be obtained. Rather, it is a technique for specifying the quality of the beam using a few mathematical parameters, which, if judiciously selected, may represent the attenuation curve in the selected material with certain fidelity but which will only approximate the true spectrum. Because of the difficulties in performing detailed spectral measurements, the transmission method is, in spite of its inherent shortcoming, an effective technique for specifying beam quality.

Recently a new model was proposed that has flexibility to represent all spectral shapes (Baker et al. 1995, Baker and Peck 1997). In this model, Schiff's expression (Schiff 1951) for the forward-directed bremsstrahlung differential in photon energy, k, is used to provide a simple expression for the photon energy fluence produced by monoenergetic electrons of total energy, E, incident on a thin target (such that changes in the electron fluence on transmission may be neglected) of thickness, δ, and atomic number, Z. Neglecting constant factors, this thin-target spectrum is given by

$$\Psi_{\delta}(k) = 2\left(1-\frac{k}{E}\right)(\ln\eta - 1) + \left(\frac{k}{E}\right)^{2}\left(\ln\eta - \frac{1}{2}\right), \tag{1-9}$$

where

$$\eta = \left\{\left(\frac{k}{2EE'}\right)^{2} + \left(\frac{Z^{1/3}}{C}\right)^{2}\right\}^{-1/2}, \tag{1-10}$$

and E' is the total energy of the final electron and C a constant to which Schiff assigned a value of 111.

It is assumed that all the bremsstrahlung produced by a medical electron accelerator is generated within a small depth, δ, of the target and that narrow-beam conditions apply; the photon energy fluence spectrum produced by a medical linear accelerator with a target thickness t can be estimated from equation (1-9) by

$$\Psi_t(k) = \Psi_\delta \exp[-\mu_t(k)t] \prod_{i=1}^{n} \exp[-\mu_i(k)t_i], \tag{1-11}$$

where $\mu_t(k)$ is the total attenuation coefficient for photons of energy, k, in the target material and $\mu_i(k)$ is the corresponding coefficient for material I, of thickness t_i, present in the machine. The objective is then to select suitable parameters for the model's spectrum to represent accurately the clinical spectra generated by the electron accelerator. The first parameter, the thickness of the inherent tungsten filter, t, with total attenuation coefficient $\mu_w(k)$, is used to account for the deviation from the thin-target model which is expected to filter the low-energy part of the spectrum too heavily. A second parameter, α, which weighs the second term of the thin-target model and is expected to take on values less than unity, is used to partly correct the over-filtering. The parameterized model's spectrum is then given by

$$\Psi(k) = \left\{ \left(1 - \frac{k}{E}\right)(\ln\eta - 1) + \alpha\left(\frac{k}{E}\right)^2 \left(\ln\eta - \frac{1}{2}\right) \right\} \exp[\mu_w(k)t]. \tag{1-12}$$

This two-parameter representation of clinical spectra was found to allow reproduction of transmission data calculated for published photon spectra to an accuracy of on average 0.3 percent. Increased flexibility in the thin-target model, both in correcting for the over-filtration of low-energy photons and also to allow improved modeling of machine head filtration, may be gained by introducing an energy-dependent correction, β/k, to the inherent filtration. A three-parameter model is then given by

$$\Psi(k) = \left\{ \left(1-\frac{k}{E}\right)(\ln\eta-1)+\alpha\left(\frac{k}{E}\right)^2\left(\ln\eta-\frac{1}{2}\right) \right\}\exp[\beta/k-\mu_w(k)t].$$

(1-13)

In order to provide an increased energy fluence at lower photon energies, the value of β is expected to be positive. This will be particularly true for lightly filtered spectra where the effects of target filtration will dominate. For heavily filtered spectra these effects will become less dominant and a negative value of β may be more appropriate to allow greater flexibility in the modeling of inherent filtration. This is true because the corrective term will then provide the same effect as a filter material, the attenuation coefficient of which monotonically decreases with photon energy. If the measurements of the relative transmission, S, through a thickness, x, of a selected filter are to be made with an air-filled ionization chamber with air-equivalent walls encased in a water-equivalent build-up material, they may be related to the photon energy fluence through

$$S(x_i) = \int_0^E \Psi(k)F(k)\exp[-\mu_f(k)x_i]dk,$$

(1-14)

where $\mu_f(k)$ is the total attenuation coefficient for the filter. The function F(k) can be represented by

$$F(k) = \gamma[\mu_{en}(k)/\rho]_w S_{a,w} + (1-\gamma)[\mu_{en}(k)/\rho]_a,$$

(1-15)

where γ is the proportion of collected charge due to electrons generated in the surrounding water-equivalent material, $S_{a,w}$ is the stopping power ratio from air to water for the secondary-electron spectrum crossing the chamber, $[\mu_{en}(k)/\rho]_w$ is the mass-energy absorption coefficient for photons of energy k in material w, and constant factors have been omitted. Although for the energy range of interest here contributions to the measured dose will generally be significant from both the build-up material and the chamber wall, the fact that values of $S_{a,w}$ and $[\mu_{en}(k)/\rho]_a/[\mu_{en}(k)/\rho]_w$ are close to unity often leads to the approximation that $\gamma=1$ for beams with maximum photon energies above 4 MeV. In order for the energy fluence to be derived from transmission measurements the total attenuation coefficient for the filter material, $\mu_f(k)$, should be monotonic over the expected range of photon energies in the spectrum to be reconstructed. To optimize the analysis, these $\mu_f(k)$ values must also provide the greatest differentiation between successive energy bins; in other words, the magnitude of $d\mu_f/dk$ must be maximized. From these considerations, the filter material used for generation of transmission data is aluminum for maximum beam energies up to and including 6 MeV and water otherwise. Having obtained the transmission curves for the source spectra, values of parameters α, β, and t are determined by minimizing the objective function

$$O(\alpha,\beta,t)=\sum_{i=1}^{n}\left\{1-\left(\int\Psi(k,\alpha,\beta,t)\exp[-\mu_f(k)x_i]dk\right)/S(x_i)\right\}^2, \tag{1-16}$$

where the summation is over the total number of filter thickness.

The main drawback of this method is that the scattered contribution from the attenuator is difficult to determine even though the ion chamber is well shielded from other sources, like the room scatter. Thus the angular distribution information is completely gone. And the charged particle contamination is always a complication if the energy is high enough.

The second method is the photoactivation method (Nath and Schulz 1976, Krmar et al. 1993). This method takes advantage of the energy-dependent cross sections of photo-nuclear reactions and the radioactive isotopes produced by these reactions. Clearly, the types and amounts of radioactivity produced by x-ray irradiation of these materials will markedly depend upon the x-ray spectrum. Since the amount of radioactivity produced in a specific foil is proportional to the convolution of the photonuclear cross section and the x-ray spectrum, analysis of the radioactivity produced in a number of foils may be used to obtain the spectrum. The first step in the determination of a high-energy x-ray spectrum by photoactivation is to irradiate a small packet of activation foils. The choice of activation foils for spectrum determination is limited by the following conditions:

(1) The specific isotope that is to be made radioactive must have a high natural abundance (>10%);
(2) For convenience, the material should be chemically stable and a solid at room temperature;
(3) The half-life of the daughter nucleus should be longer than 5 minutes and shorter than 100 days.

(4) The daughter nucleus should emit gamma rays of known energy and branching ratio; also, the branching ratio for gamma ray emission must be large.

(5) The gamma ray spectrum must not be too complex for accurate activity measurements using a spectrometer;

(6) Competition between x rays and photoneutrons for the production of the same daughter nucleus should strongly favor x rays.

The orthonormal expansion technique is then employed for the unfolding of x-ray spectra from the measured activity data. The differential photon fluence Φ(E), with the dimensions of photons/cm^2 sec MeV interval, is expanded into a series of linearly independent orthonormal functions $\psi_l(E)$ as follows:

$$\Phi(E) = W(E)\sum_{l=1}^{n} a_l \psi_l(E), \tag{1-17}$$

where n is the number of activation foils, W(E) is a weighting function, and a_l is the expansion coefficient. The reaction probability per second per nucleus, R_j, for the jth activation foil, having a photonuclear cross section $\sigma_j(E)$, is given by

$$R_j = \int_0^{\infty} \Phi(E)\sigma_j(E)dE. \tag{1-18}$$

In practice, the limits of the integration can be reduced from (0, ∞) to (E_{0j}, E_{max}) because the cross section beyond this range is zero, where E_{0j} is the threshold energy for photonuclear reaction and E_{max} is the maximum photon energy in the x-ray spectrum.

Combining Eqs. (1-17) and (1-18) results in

$$R_j = \sum_{l=1}^{n} a_l S_{lj}$$

where

$$S_{lj} = \int_{E_{0j}}^{E_{\max}} W(E)\psi_l(E)\sigma_j(E)dE.$$

(1-19)

The integrals of S_{lj} are determined by the choice of weighting function W(E), polynomial $\psi_l(E)$, and the photonnuclear cross section of foil j, $\sigma_j(E)$. Therefore, as the values of R_j are measured quantities, Eq. (1-18) can be solved for the expansion coefficient a_l for the solution of Eq. (1-17). Inasmuch as all high-energy bremsstrahlung spectra have similar shapes, the theoretical thin-target spectrum of Schiff is used as the weighting function and the Laguerre, Legendre, or Chebyshev polynomials can be used for orthonormal expansion.

The main shortcomings of this method are first, the high threshold energies thus lower energy region of the spectrum cannot be determined by this method, and second, the contributions of competing reactions are difficult to assess and then to eliminate. Also, the accuracy of this method is strongly dependent on the availability and accuracy of the photo-activation cross section data of the nuclides chosen to be irradiated.

The Monte Carlo simulation technique has found widespread application in the radiological sciences (Morin 1988). The use of Monte Carlo applications in medical physics has been reviewed by Mackie (1990) and Andreo (1991). This expanded utilization is due to the available computing power and the accessibility of software packages (e.g., EGS4/BEAM, GEANT, MCNP, etc).

Direct Monte Carlo simulations of the treatment head design have been carried out by several researchers in order to provide spectral data. For a series of beam energies Mohan et al. (1986) calculated spectra that later were frequently used as a standard set. They also studied the lateral variation in beam spectrum and characterized it in terms of half-value thickness. Lovelock et al. (1995), Liu et al. (1997) and DeMarco et al. (1998) applied Monte Carlo techniques to generate beam spectra and all found that the incident electron beam energy must be tuned in order to get agreement with measured depth dose data.

The EGS Monte Carlo code was used by Han et al. (1987) to compute photon spectra from an AECL Theratron 780 cobalt-60 unit. They concluded that the observed increase in output of the machine with increasing field size is caused by scattered photons from the primary definer and the adjustable collimator of the unit. They also showed the spectrum photons reaching the surface of a patient for a fixed source-to-surface distance (SSD). It is known that the energy spectrum consists not only of the 1.17- and 1.33-MeV primary photon lines, but also of a broad distribution of photons of lower energies resulting mainly from Compton interactions. These spectra were then used as input to a pencil-beam model to calculate tissue-air ratios in water. This result was compared with a calculation which assumes a monochromatic photon energy of 1.25 MeV and measured data. The agreement among the three curves was good up to a depth of 10 cm. Beyond that point, the dose contribution calculated for 1.25 MeV photons is higher than the dose calculated using a more realistic spectrum. The authors inferred that one possible reason for this discrepancy was that they used parallel beams for the calculation, while for the measured data the beam is divergent. Recently, Mora (1999) used the BEAM (Rogers 1995) Monte Carlo code to simulate the cobalt-60 beam from an Eldorado 6 radiotherapy unit and to calculate the relative air-kerma output factors as a function of field size. This unit is more realistically modeled. The calculated relative air-kerma output factors at SSD=80.5 agree to within 0.1% with measured values. It is shown that the variation of the output factor is almost entirely due to scattered photons from the fixed and adjustable collimators and there is no effect of shadowing primary photons. The influence of the geometry of the collimating system on the photon spectra on-axis is shown to be small but finite. The calculated buildup region of a depth-dose curve in a water phantom irradiated by a narrow and broad cobalt-60 beam is shown to agree with experimental data at the 2% and 3% levels. Unlike previous calculations, their results accurately predict the effects of electron contamination from the surface to dose maximum. The field size is shown to have some effect on the photon spectra.

The MCNP (Briesmeister 1997) Monte Carlo code has been employed by Lewis (1999) to calculate the energy spectra and angular distributions of x-ray beam for the Philips SL75/5 linear accelerator in a plane immediately beneath the flattening filter. These data were subsequently used as a "source" of x-rays at the target position, to assess the emergent beam from the secondary collimators. The depth dose distribution and dose profiles at constant depth for various field sizes have been calculated for a nominal operating potential of 4 MV and found to be within acceptable limits. Analysis of the x-ray spectra shows that the energy-weighted mean energy (i.e., the relative number of x rays in each interval multiplied by their energy) leaving the target, the primary collimator, flattening filter, and secondary collimators is 1.16, 1.32, 1.31, and 1.28 MeV, respectively, assuming a secondary collimating setting of 10 by 10 cm (field size of 14.5 cm2 at 100 cm SSD). The overall mean x-ray energy of the emergent beam from the secondary collimators, 1.28 MeV, agrees with the generally perceived value of one-third the maximum energy. In the central part of the beam, as expected, the flattening filter has the largest influence on hardening. The variation in fluence-weighted x-ray energy with radial distance of the filtered and unfiltered 4 MV beams was also compared. The result showed that the filtered and unfiltered beams had approximately the same fluence-weighted x-ray energy at a distance of 4 cm away from the central axis within the linear accelerator head and also the preferential filtration of the lower energy components by the filter.

The principal advantage of the Monte Carlo method is that it can be used to obtain angular distributions, quantities that can hardly be measured experimentally. The second advantage is that the energy spectrum can be generated in regions away from the central axis simultaneously. The third advantage is the possible savings in manpower at the expense of large amounts of CPU time of computers. In theory, this method provides an accurate means of obtaining the energy spectrum and angular distributions. In addition, the Monte Carlo method can be used to simulate the energy distribution and angular distribution of electrons, thus providing insights on electron contamination on photon beams or photon contamination on electron beams (Petti 1983a, 1983b). The accuracy of the Monte Carlo method is limited to the modeling of the machine head construction and assumptions made concerning the electron beam incident on the target, pre-assuming that the particle transport models including cross section data are accurate. The drawback of such simulation is the lack of traceablity to measured quantities.

The fourth method is the incoherent scattering method. This method has been tried on several occasions in the past to deduce the energy spectra (Bentley et al. 1967, Levy et al. 1974, 1976, Faddegon et al. 1990, 1991, Landry and Anderson 1991). In this method, a small scattering material is put in the beam, and the once-scattered spectrum is then measured at a certain angle, so that from the scattered spectrum it is relatively simple to deduce the original spectrum. The scattered radiation intensity incident on the detector is reduced by several magnitudes by the scattering process; furthermore, the energy of the scattered photons is reduced as well because of the incoherent scattering, so that a more suitable detecting energy range for the detector is obtained. And the detector can accept radiation from the interior of the beam-defining system as well as from the source. The angular distribution of photons can be measured by scanning the small scatter in the radiation field. Most of the measurement were done with NaI(Tl) detectors, but the poor resolution inherent to this type of spectrometer renders the information less valuable. With the advent of the HPGe detector, its superb energy resolution provides an ideal technique for accurate measurement of spectral information for x rays.

A drawback of the incoherent scattering method is that, as the higher energy photons have a smaller probability of being scattered than do the lower energy photons and suffer a greater fractional decrease in their energy on incoherent scattering, this method results in a reduction of resolution. To demonstrate this effect quantitatively, a mono-energetic source and a spectrometer with good spectral resolution are needed. This effect is demonstrated clearly with a cobalt-60 teletherapy unit using HPGe detector. Also, in the incoherent scattering method, it is necessary to define an accurate scattering angle. This procedure needs a collimator which can not only cause distortions in measured spectrum, but increase the difficulty in alignment as well.

In order to fully understand the reliability, the applicability and the limitations of the incoherent scattering method, a series of Monte Carlo simulations and measurements are performed with a cobalt-60 therapy machine and medical linear accelerators. To describe quantitatively the loss of resolution inherent to this method, the "broadening factor" is introduced. Its effects on line spectrum and continuous spectrum are assessed to improve the accuracy of the measured spectra.

CHAPTER 2
THEORY OF INCOHERENT SCATTERING METHOD

Scattering

The theory of scattering method is based on two major scattering types: coherent and incoherent scattering. If $I(E_o)$ photons/sec of energy E_o are incident on the scattering material with atomic number Z and thickness Δx, then the number D(E) of photons/sec scattered at a certain angle θ and incident on a detector which subtends solid angle $d\Omega$ (ignoring the attenuation in the scatter itself if the scatterer is small) is given by:

$$D(E)dE = [N\Delta x\Delta\Omega\varepsilon(E)](\frac{d\sigma_{Coh}}{d\Omega} + \frac{d\sigma_{Incoh}}{d\Omega})I(E_o)dE_o, \tag{2-1}$$

where E_o and E are the energies of the incident and once-scattered photons, Z is the atomic number of the scattering material Δx is the thickness of the scatterer, N is the number of atoms in the relevant scattering volume, $\varepsilon(E)$ is the efficiency of the detector, and $\Delta\Omega$ is the solid angle subtended by the pinhole of the collimator in front of the detector. The atomic differential coherent scattering cross section and incoherent scattering cross section are given below:

$$\frac{d\sigma_{Coh}}{d\Omega} = \frac{r_0^{\ 2}(1+\cos^2\theta)}{2} F^2(x,Z),$$

(2-2)

$$\frac{d\sigma_{Incoh}}{d\Omega} = \frac{d\sigma_{KN}}{d\Omega} S(x,Z) = \frac{r_0^{\ 2}}{2}\left(\frac{E}{E_0}\right)^2 \left(\frac{E}{E_0} + \frac{E_0}{E} - \sin^2\theta\right) S(x,Z),$$

(2-3)

where $r_0 = 2.818 \times 10^{-13}$ cm is the classical radius of the electron, $x = \sin(\theta/2)/\lambda$ is the momentum transfer parameter, λ is the wavelength of the incident photons, θ is the scattering angle of the photon, defined as the angle between the direction of flight before and that after the interaction, $d\Omega = 2\pi \sin\theta d\theta$ is the solid-angle element, F(x, Z) is the atomic form factor, and S(x, Z) is the incoherent scattering function.

Coherent Scattering

For low-energy photons or small-angle scattering, the energy transferred to the struck electron is small compared with the binding energy of the electron. The atom is neither ionized nor excited, and the recoil momentum is absorbed by the entire atom. Under these conditions, the energy of the photon scattered by the bound electrons of an atom is essentially the same as that of the incident photon, and no energy is deposited. There is a fixed phase relationship among the scattered x rays, which are thus capable producing constructive interference. This process is called coherent scattering or Rayleigh scattering. It is most prominent for low-energy photons scattered in high Z materials. Eq. (2-2) gives the atomic differential cross section per atom for unpolarized radiation. F(x, Z) is the atomic form factor that can be theoretically calculated by partially-relativistic or relativistic quantum mechanics. While Hubbel (1975) complied the partially-relativistic quantum mechanics calculation results, more accurate and complete compilation was done by Chantler (1995). Figure 2-1 shows the atomic form factors of carbon (Z=6) and lead (Z=82). As can be seen, F(x, Z) is approximately equal to Z for momentum transfers smaller than that typical of orbital electrons. As the momentum transferred exceeds this

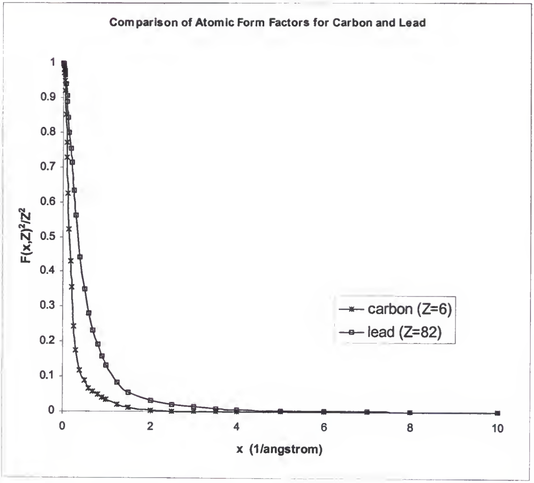

Figure 2-1. Atomic form factor versus momentum transfer parameter for elements carbon and lead (normalized to Z^2)

typical value, the electrons are less likely to scatter photons elastically, causing the form factor to fall off rapidly with increasing scattering angle and incident photon energy. The result is a highly anisotropic, forward-peaked angular scattering distribution. The square of the atomic form factor F(x,Z) represents the probability that the Z electrons take up the recoil momentum, without absorbing any energy from the photon.

Incoherent Scattering

Incoherent scattering, often identified with the Compton effect, is an inelastic collision between an atom and an x-ray photon in which the orbital electrons retain part of the photon energy, altering both the energy and flight path of the incident photon. For small scattering angle and low-energy incident x-rays, the recoil energy of the electron would be comparable to or smaller than the electron binding energy, especially for heavy elements. Thus, the assumption that the electron is initially free and stationary may not apply. The deviation from the free electron cross section is greatest for the inner-shell electrons and becomes negligibly small for the loosely bound valence electrons. Therefore, the correction to the Klein-Nishina collision cross section depends upon the atomic number Z and should be expressed on a per-atom basis. To a close approximation, the probability can be expressed as the product of the Klein-Nishina cross section and the incoherent scattering function, S(x, Z), which is shown by Eq. (2-3). The latter factor represents the probability that an atom will be raised to any excited or ionized state when a photon imparts a recoil momentum to an atomic electron. The momentum transfer parameter is given by

$$x = \frac{m_o c}{2h}[E_o{}^2 + E^2 - 2E_o E\cos\theta]^{1/2}, \tag{2-4}$$

where m_o, c, and h denote electron rest mass, velocity of light, and Planck's constant, respectively. Since the binding corrections are only important for small momentum transfers, an approximation is often made for the purpose of computing x. This allows use of the simple expression, $x=\sin(\theta/2)/\lambda$, for both coherent and incoherent scattering. The error introduced into the differential cross section by this approximation does not exceed 1-2% (Williamson 1984). The incoherent scattering function can therefore be expressed in terms of the same variable, x, defined previously for the form factors. The incoherent scattering functions have been tabulated along with atomic form factors for all elements (Hubbell 1975, Chantler 1995). The factor S(x, Z) increases rapidly, especially for low Z elements, at small values of x and approaches a maximum value of Z at large values of x. Therefore, the incoherent scattering function modifies the Klein-Nishina cross section most prominently for small-angle scattering of low energy photons in high Z elements, i.e., under conditions where the effect of electron binding is strong. Figure 2-2 shows the incoherent scattering functions for carbon and lead plotted as a function of x. These curves illustrate the dependence of the effect of electron binding on the atomic number.

The electron binding effect also introduces a small deviation in the Compton energy shift of the photon. Since the effective mass of a bound electron tends to be slightly increased, the energy transferred to a bound electron is less than that transferred to a free electron. Nevertheless, this change in energy shift is negligibly small, so that modification of the angular distribution of the scattered photon alone will be adequate in a photon diffusion model.

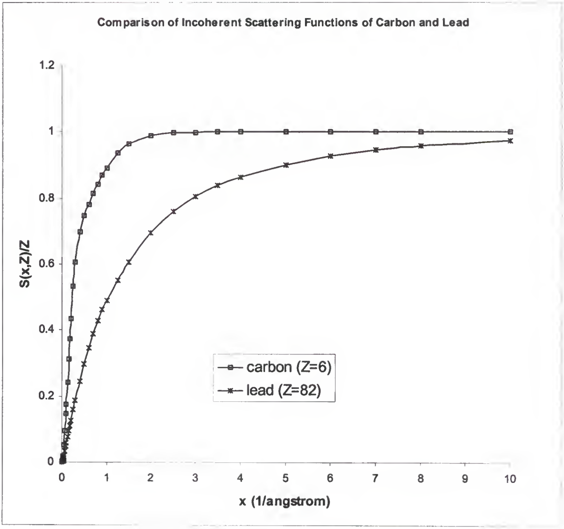

Figure 2-2. Incoherent scattering functions versus momentum transfer parameter for elements carbon and lead (normalized to Z)

The original spectrum incident on the scatter can then be deduced by rearranging terms from Eq. (2-1):

$$I(E_o)=\left(\frac{D(E)}{[N\Delta x\Delta\Omega\varepsilon(E)]\dfrac{d\sigma_{Coh}}{d\Omega}}\right)\frac{dE}{dE_o}+\left(\frac{D(E)}{[N\Delta x\Delta\Omega\varepsilon(E)]\dfrac{d\sigma_{Incoh}}{d\Omega}}\right)\frac{dE}{dE_o}.$$

(2-5)

In the case of insignificant coherent scattering, Eq. (2-5) is reduced to:

$$I(E_o)=\left(\frac{D(E)}{[N\Delta x\Delta\Omega\varepsilon(E)]\dfrac{d\sigma_{Incoh}}{d\Omega}}\right)\frac{dE}{dE_o}=\left(\frac{D(E)}{[N\Delta x\Delta\Omega\varepsilon(E)]\dfrac{d\sigma_{Incoh}}{d\Omega}}\right)\left(\frac{E}{E_o}\right)^2.$$

(2-6)

Choice of Scattering Angle

The scattered photon energy after the scattering process is given by the Compton energy-angle relation:

$$E=\frac{E_0}{1+\dfrac{E_0}{m_0c^2}(1-\cos\theta)}.$$

(2-7)

As the incident energy becomes very large compared with the rest mass energy of the electron, Eq.(2-7) can be approximated by:

$$E=\frac{m_0c^2}{1-\cos\theta}.$$

(2-8)

For a scattering angle of 30°, the scattered photon energy range is between 0 and 3.8 MeV; for a scattering angle of 60°, the scattered photon energy range is between 0 and 1.022 MeV; and for a scattering angle of 90°, the scattered photon energy range is between 0 and 0.511 MeV. Thus we can see that the incoherent scattering process squeezes the original spectrum to a narrower range, this "shrinkage effect" is more evident with larger scattering angles. To minimize the effect, a smaller angle is preferred. On the other hand, detector calibration and detecting efficiency considerations include:

a. suitable gamma sources for detector efficiency calibration are not available for higher energies;

b. the detection efficiency of germanium spectrometers decreases rather rapidly for photons of energy above a few MeVs.

Because of these two conflicting requirements, a compromise must be reached. With the use of Eq. (2-6), the scattering angle that yields a maximum energy can be calculated as follows:

$$\cos\theta = 1 + \frac{m_o c^2}{E_o} - \frac{m_o c^2}{E}, \tag{2-9}$$

where the E_o is the end point energy of the spectrum, and E is the upper limit of the scattered spectrum. For preliminary analysis, E assumes a value of 2 MeV, 1.5 MeV, 1.0 MeV, and 0.511 MeV, respectively. The calculated results are shown in

Table 2-1. These angles are the minimum angles required to ensure that the scattered spectrum lies in the range of 0 to E for an incident spectrum with maximum energy E_o.

Table 2-1. Minimum scattering angles (in degree).

E	2 MeV	1.5 MeV	1.0 MeV	0.511 MeV
Eo (keV)				
1000			0.0	59.26954
3000	23.81793	33.93549	48.75095	80.1928
5000	32.14546	40.40044	53.75779	84.13413
7000	35.16469	42.91764	55.80578	85.81369
9000	36.74771	44.26567	56.92217	86.74512
11000	37.7252	45.10677	57.62526	87.33739
13000	38.38946	45.68193	58.10882	87.74726
15000	38.87047	46.10015	58.46182	88.04775
17000	39.23495	46.41799	58.73086	88.2775
19000	39.5207	46.66774	58.94272	88.45886
21000	39.75076	46.86916	59.11388	88.60567
23000	39.93998	47.03506	59.25505	88.72693
25000	40.09835	47.17407	59.37347	88.82879

This can also be presented in a graph, which is shown in Figure 2-3.

Effect of Collimator

A collimator is used in front of the detector to define the scattering angle. The effect of the collimator on the detected energy spectrum has two effects. The first one is the buildup effect which is dependent on the material that the collimator is made of and the incident spectrum. The secondary photons (including degraded photons, bremsstrahlung photons, and characteristic x rays) from the edge of the collimator

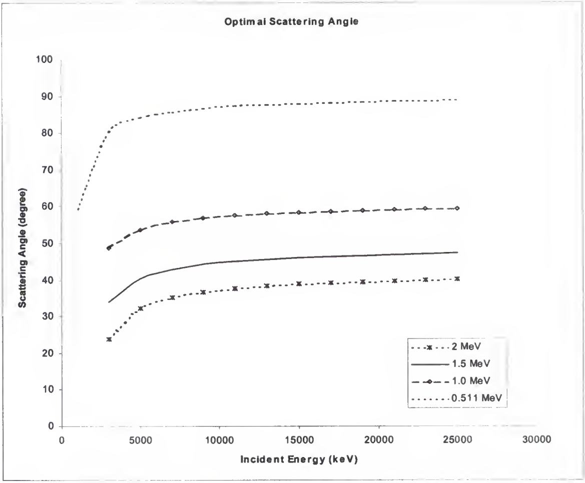

Figure 2-3. Optimal scattering angle for different detecting scattered energy ranges and incident photon energy.

will deform the incident spectrum. Because this effect is difficult to demonstrate analytically, the Monte Carlo technique is a good method to show the effect directly. The second effect is the scattering angle. To make the scattering angle as accurate as possible, the radius of the pinhole in the collimator should be as small as possible. In practice, pinhole is of finite size, causing the scattered photons to have a small spread in their energies. This is defined as the geometric line-broadening effect. The severity of this effect can be calculated with the aid of differentiation of the Compton energy-angle relation:

$$dE = \frac{m_o c^2}{\left[1 + \frac{m_o c^2}{E_o} - \cos\theta\right]^2} d(\cos\theta).$$

(2-10)

The results are shown in Table 2-2, Table 2-3, and Table 2-4 respectively, for monoenergetic photons with energies of 100 keV, 1000 keV, and 10 MeV, at different scattering angles.

Table 2-2. The geometric line broadening (in keV) of 100 keV photons

Scattering angle*	15	30	60	90	120	150
Deviation* from scattering angle						
0	0.0	0.0	0.0	0.0	0.0	0.0
0.1	0.008723	0.016216	0.024542	0.02389	0.017678	0.009163
0.2	0.017447	0.032432	0.049083	0.04778	0.035355	0.018327
0.3	0.02617	0.048648	0.073625	0.07167	0.053033	0.02749
0.4	0.034893	0.064865	0.098166	0.09556	0.070711	0.036653
0.5	0.043616	0.081081	0.122708	0.11945	0.088389	0.045817
0.6	0.05234	0.097297	0.14725	0.14334	0.106066	0.05498
0.7	0.061063	0.113513	0.171791	0.16723	0.123744	0.064143
0.8	0.069786	0.129729	0.196333	0.19112	0.141422	0.073306
0.9	0.07851	0.145945	0.220875	0.21501	0.159099	0.08247
1	0.087233	0.162161	0.245416	0.2389	0.176777	0.091633

*Scattering angle and deviation are both in degrees

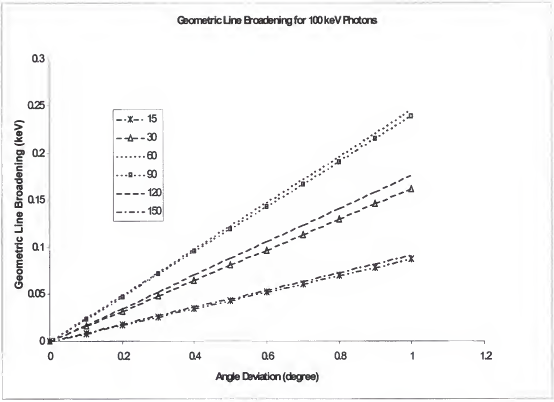

Figure 2-4. Geometric line broadening for 100 keV photons.

Table 2-3. The geometric line broadening (in keV) of 1000 keV photons

Scattering angle*	15	30	60	90	120	150
Deviation* from scattering angle						
0	0.0	0.0	0.0	0.0	0.0	0.0
0.1	0.776932	1.071971	0.75566	0.390633	0.190987	0.078922
0.2	1.553865	2.143942	1.511321	0.781267	0.381975	0.157845
0.3	2.330797	3.215913	2.266981	1.1719	0.572962	0.236767
0.4	3.10773	4.287884	3.022641	1.562534	0.76395	0.31569
0.5	3.884662	5.359855	3.778301	1.953167	0.954937	0.394612
0.6	4.661595	6.431826	4.533962	2.3438	1.145925	0.473535
0.7	5.438527	7.503797	5.289622	2.734434	1.336912	0.552457
0.8	6.21546	8.575768	6.045282	3.125067	1.527899	0.63138
0.9	6.992392	9.647739	6.800942	3.5157	1.718887	0.710302
1	7.769325	10.71971	7.556603	3.906334	1.909874	0.789225

*Scattering angle and deviation are both in degrees.

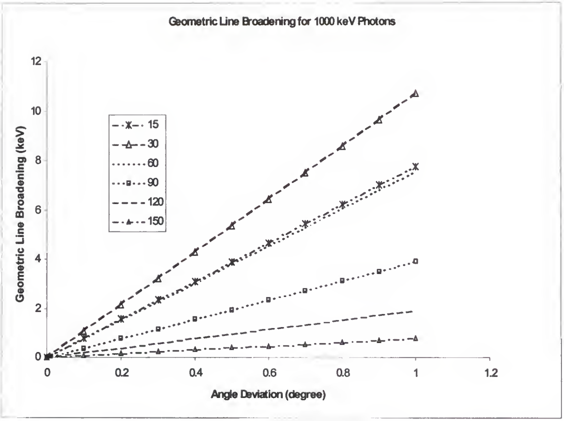

Figure 2-5. Geometric line broadening for 1000 keV photons.

Table 2-4. The geometric line broadening (in keV) of 10 MeV photons

Scattering angle*	15	30	60	90	120	150
Deviation* from scattering angle						
0	0.0	0.0	0.0	0.0	0.0	0.0
0.1	31.81842	13.01891	2.543127	0.807254	0.321033	0.12133
0.2	63.63684	26.03782	5.086254	1.614508	0.642065	0.242659
0.3	95.45527	39.05673	7.629382	2.421762	0.963098	0.363989
0.4	127.2737	52.07564	10.17251	3.229016	1.284131	0.485319
0.5	159.0921	65.09455	12.71564	4.03627	1.605164	0.606649
0.6	190.9105	78.11347	15.25876	4.843524	1.926196	0.727978
0.7	222.729	91.13238	17.80189	5.650778	2.247229	0.849308
0.8	254.5474	104.1513	20.34502	6.458032	2.568262	0.970638
0.9	286.3658	117.1702	22.88815	7.265286	2.889295	1.091968
1	318.1842	130.1891	25.43127	8.07254	3.210327	1.213297

*Scattering angle and deviation are both in degrees.

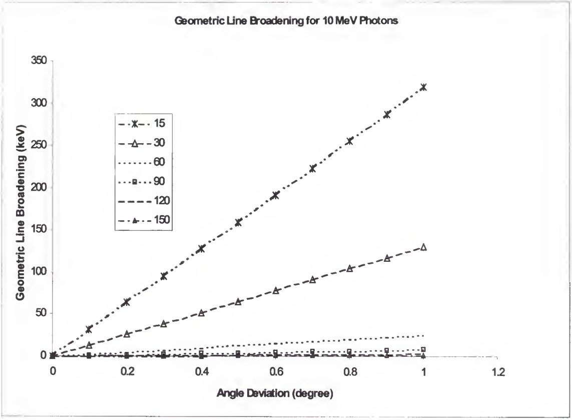

Figure 2-6. Geometric line broadening for 10 MeV photons

From Tables 2-2 to 2-4, it is shown that the geometric line broadening of the scattered spectrum due to the deviation of scattering angle can be significant. Care should be taken in actual experiments to make sure that the deviation from the specified scattering angle is minimized.

The choice of the collimator materials, which is discussed in the next section, follows essentially the same principles that need to be followed for shielding materials. Depending on the actual situation, the design of the collimator is also important.

Choice of Shielding Materials

Shielding materials are needed for both photons and neutrons. The commonly used photon shielding material is lead, the cross section of which is shown in Figure 2-7. From Figure 2-7 we see that, below 0.4 MeV, the predominant mode of interaction is the photoelectric effect, which means if the primary photon energy is degraded to below 0.4 MeV, there is an almost certain likelihood that photons will be

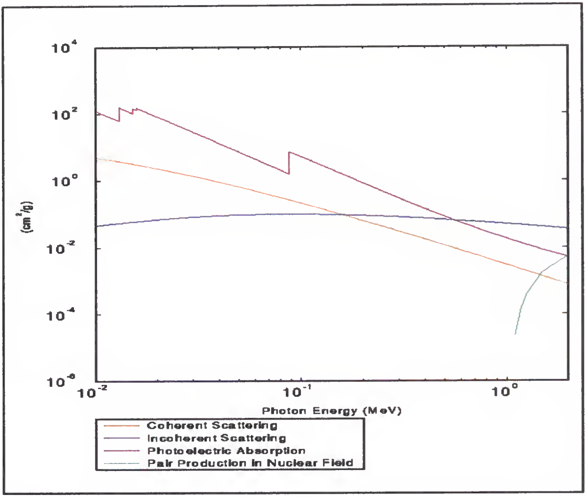

Figure 2-7. The photon cross sections for lead

absorbed, generating characteristic x rays. These characteristic x rays, even if they can make it to the detector, can be distinguished easily causing little complication. Depending on the photon energy, the required thickness of lead can be readily estimated.

Photoneutrons generated by (γ,n) reactions in a high energy x-ray radiation field can be annoying and proper attention should be paid to eliminate their effects. Neutrons are known to activate not only Ge crystal in the detector, but surrounding materials as well, complicating the response of the spectrometer. The induced radioactivity can cause severe pile-up problems in some cases. Polyethene has been tried as a neutron shield; it can serve this purpose well.

Choice of Scattering Material

Ideally, from Eq. (2-4), we would like to have only incoherent scattering so that the process of deducing the original spectrum is easier. This condition can be met at high energies and large scattering angles. For low Z materials, Compton scattering is a very good approximation of incoherent scattering under the above-mentioned conditions. This approximation greatly simplifies the process, as the atomic number Z can be used to replace the incoherent scattering function S(x, Z), the Compton energy-angle relation can be used to deduce the energy, and the well-known Klein-Nishina formula can be used to obtain the differential probability. Usually the Compton scattering cross section in low Z materials at high energies is large, which makes them very suitable for scattering purposes. For example, for carbon, for photon energies between several hundred keV up to a few MeV, the Compton process is predominant, the photoelectric effect in this energy range is negligible, and pair production amounts to only a small percent of the total cross section. The photon differential atomic coherent and incoherent scattering cross sections for several scattering angles with three different energies are shown in Figures 2-8 to 2-10. In comparison, the photon cross sections for lead under the same conditions are shown in Figures 2-11 to 2-13. These data clearly show the advantage of low Z materials as scatters if Compton scattering is desired.

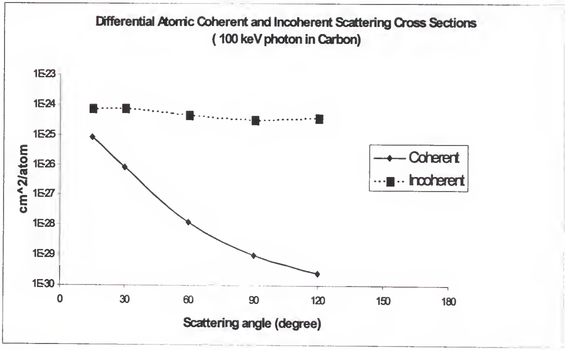

Figure 2-8. Differential atomic coherent and incoherent cross sections for 100 keV photons in carbon.

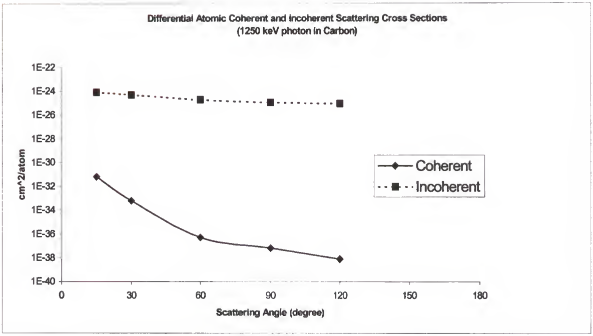

Figure 2-9. Differential atomic coherent and incoherent cross sections for 1250 keV photons in carbon.

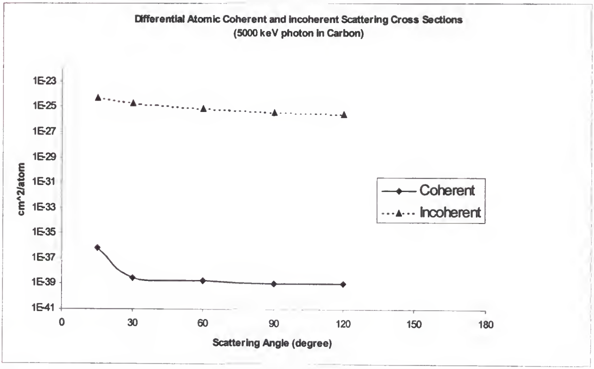

Figure 2-10. Differential atomic coherent and incoherent cross sections for 5000 keV photons in carbon.

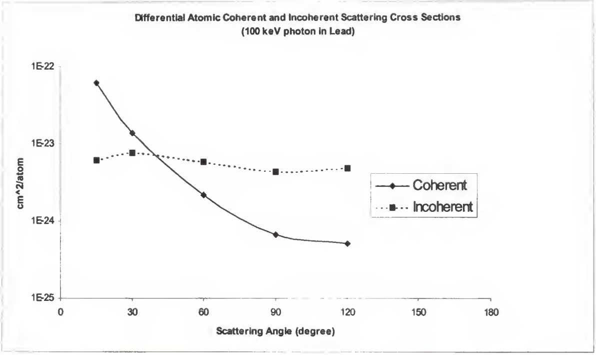

Figure 2-11. Differential atomic coherent and incoherent cross sections for 100 keV photons in lead.

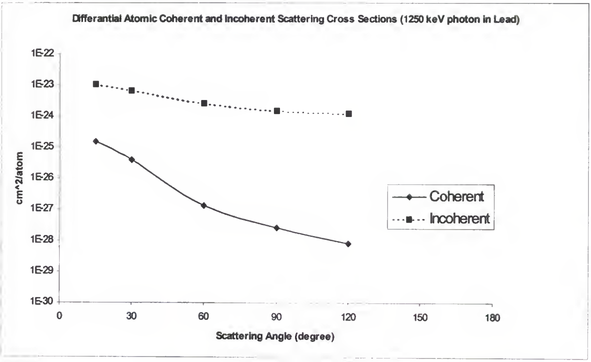

Figure 2-12. Differential atomic coherent and incoherent cross sections for 1250 keV photons in lead.

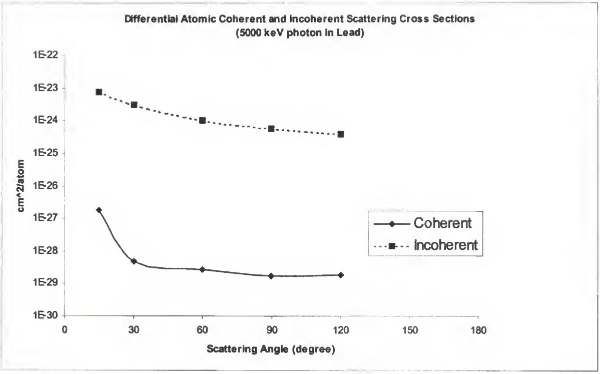

Figure 2-13. Differential atomic coherent and incoherent cross sections for 5000 keV photons in lead.

Detector Response

Of the various ways gamma rays can interact in matter, only three interaction mechanisms have any significance in gamma ray spectroscopy. These are photoelectric absorption, Compton scattering, and pair production. The effect of photoelectric absorption is the liberation of a photon-electron, which carries off most of the gamma-ray energy together with one or more low-energy electrons corresponding to the absorption of the original binding energy of the photon-electron. If nothing escapes from the detector, then the sum of the kinetic energies of the electrons that are created must be equal to the original energy of the gamma-ray photon. Photoelectric absorption is therefore an ideal process if one is interested in measuring the energy of the original gamma rays. The total electron kinetic energy equals the incident gamma-ray energy and will always be the same if monoenergetic gamma rays are involved. The result of a Compton scattering interaction is the creation of a recoil electron and scattered gamma-ray photon, with the division of energy between the two depending on the scattering angle. In normal circumstances, all scattering angles will occur in the detector. Therefore, a continuum of energies can be transferred to the electron, ranging from zero up to the maximum recoil energy occurred at 180° scattering. The pair production occurs in the Coulomb fields of a nucleus or an electron of the absorbing material and corresponds to the creation of an electron-positron pair at the point of complete disappearance of the incident gamma-ray photon. Because an energy of two times the rest mass energy of an electron is required to create the electron-positron pair, a minimum gamma-ray energy of 1.022 MeV is required to make the process energetically possible. If the incident gamma-ray energy exceeds this value, the excess energy appears in the form of kinetic energy shared by the electron-positron pair. A plot of the total (electron + positron) charged particle kinetic energy created by the incident gamma-ray is again a simple delta function, only 1.022 MeV below the incident gamma-ray energy. The pair production is complicated by the fact that the positron is not stable. Once its kinetic energy becomes very low (comparable to the thermal energy of normal electrons in the absorbing material), the positron will annihilate or combine with a normal electron in the absorbing medium. At this point both disappear, and they are replaced by two annihilation photons of energy 0.511 MeV each.

As discussed above, the preferred mode of interaction is photoelectric absorption in gamma-ray spectroscopy with monoenergetic energy peaks. However, the predominant interaction mode of germanium in the energy range of 0.2 to 2.0 MeV is Compton scattering. Because the ratio of the Compton scattering to the photoelectric cross section is large, a much greater fraction of all detected events lies within the continuum rather than under the photopeak.

In any normal detector, the measured spectrum consists of a photopeak (full energy deposition), a Compton edge, a Compton continuum, and the continuum between photopeak and Compton edge, which is due to multiple Compton scattering. If the energy is high enough to make pair production occur, a single escape peak and/or double escape peak will be observed. Other complications include escape of secondary electrons, escape of bremsstrahlung, and escape of characteristic x rays. Sometimes the surrounding materials near the detector will have an influence on the observed spectrum in the form of back-scattered peak, annihilation peak, or characteristic x-ray peak. Summation peaks can also be seen occasionally.

For the usual geometry in which the gamma rays are incident externally on the surface of the detector, some interactions taking place near the surfaces of the detector will have a bigger probability of partially losing energies, thus complicating the response function. The response function to be expected for a real gamma-ray detector will depend on the size, shape, and composition of the detector, and also on the geometric details of the irradiation conditions.

All the discussions above are only applicable to monoenergetic photons. For any x rays with a certain spectrum, the response function of the detector is more complicated and can only be adequately predicted by using the Monte Carlo method.

CHAPTER 3
MATERIALS AND METHODS

Several experiments have been conducted to test the incoherent scattering method and to calibrate the measurement setup; the complications from the collimators are also verified with the same detecting system.

Cobalt-60 Therapy Machine

A typical cobalt -60 therapy machine consists of the following:

1. an encapsulated radioactive source,
2. a source shielding or housing,
3. a shutter device to turn the beam on and off,
4. a collimating system to limit the size of the beam,
5. a support mechanism by which the beam can be oriented with respect to the volume to be treated, and
6. ancillary devices attached to the source shield or the support mechanism to facilitate beam alignment or other clinical procedures.

Cobalt is a brittle, hard, ferromagnetic metal having an atomic weight of 58.94, a density of 8.9 g/cm^3, and the atomic number 27. Cobalt-60 can be readily produced by neutron irradiation of cobalt-59 in a nuclear reactor. It is known that the attainable specific activity is strongly dependent upon neutron flux. Efficient production of high-specific activity sources for cobalt-60 teletherapy can be achieved only in reactor positions in which the flux is 10^{13} neutrons per square centimeter per second or higher.

Cobalt-60 decays to nickel-60 with the emission of beta particles with a maximum energy 0.32 MeV and two photons per disintegration of energies 1.172 and 1.332 MeV. Sources today are made of nickel-cobalt alloy to eliminate dusting and corrosion. These high-specific activity pellets are doubly encapsulated. Both inner and outer capsules are of low carbon stainless steel and are sealed by heliarc welding. This kind of encapsulation enables the production of 1.5 cm and 2.0 cm sources with outputs up to 250 R/min at 1 meter (Rmm). The beta particles are absorbed in the cobalt and nickel metal and the resulting capsules emit bremmstrahlung x rays and a small amount characteristic x rays. These low energy x rays are strongly attenuated and do not contribute appreciably to the dose in the patient.

The shielding of the high-specific activity becomes important to make sure that the source is placed in a safe condition (i.e., with the shutter closed). Conservatively, the leakage radiation from the source shielding will average less than 2 mR/hr at a distance of 1 meter from the source in all directions, and will nowhere exceed 10 mR/hr at this distance. For a source at the kilocurie range of activity, this requires an attenuation factor of about 10^6, or approximately 20 half-value thicknesses (HVT).

A shutter is a general term describing the means by which the useful beam of radiation can be interrupted. It is imperative that in the event of power failure the unit immediately returns to the "off" position. An auxiliary safety feature which should be included is a means by which manual closing of the shutter is possible.

An integral part of the shutter system is the timing device that terminates the exposure. Since the dose rate can be determined to a high degree of precision for any set of treatment conditions, the exposure time is the all-important parameter in treatment. Thus the timer must be accurate and unfailing in its operation, and must be designed so as to minimize "operator error."

The purpose of the collimating system is to permit the useful beam to be shaped to fit the treatment volume. To be practical a collimator should be designed to permit all possible rectangular fields from 4 by 4 cm to 35 by 35 cm. In addition, complex fields shaped for the individual patient by the use of additional shielding blocks placed on a tray under the collimator are also needed. The simplest form of continuously adjustable diaphragm consists of two pairs of heavy metal blocks. Each pair can be moved independently so as to be able to obtain a square or a rectangular-shaped field. Some collimators are multi-vane type. In either case, the radiation will pass through the edges of the collimating blocks, resulting in what is known as the transmission penumbra and secondary interactions which produce scattered photons and electrons. It is now known that the collimating system is the main reason for the heterogeneity of the radiation beam from a cobalt-60 machine.

The Theratron 1000 (MDS Nordion) cobalt-60 therapy machine is used , its energy spectrum is measured using the scattering method, the scattered spectrum is transformed back to the original spectrum and compared with the known cobalt-60 spectrum.

High Purity Germanium Detector

In gamma ray spectroscopy, greater detector volume is preferred for two reasons. First, using a larger detector the response function can be simpler, and second, higher energy gamma rays can be detected with greater efficiency. One approach taken to achieve large detector volume is to reduce the impurity concentration. Techniques have been developed to reduce the impurity concentration to approximately 10^{10} atoms/cm^3 in germanium. Detectors that are manufactured from this ultrapure germanium are called high-purity germanium (HPGe) detectors. The HPGe detectors can have either planar or coaxial configuration. Because of the small bandgap (0.7 eV), room-temperature operation of germanium of any type is impossible because of the large, thermally induced leakage current that would result. Instead, germanium detectors must be cooled and normally, an insulated dewar in which a reservoir of liquid nitrogen is used which is in thermal contact with the detector.

The high-purity germanium detector (HPGe) has the advantages of excellent energy resolution, high detecting efficiency, and ease of use. We have used an HPGe from EG&G Ortec. The diameter of the Ge crystal is 5.0 cm and the thickness is also 5.0 cm. The aluminum thickness is 1.27 mm. The detector operates at a positive 2500 V bias. The measured full width at half-maximum (FWHM) resolution of the detector and the electronics is about 1.6 keV at 1330 keV. The relative efficiency at this energy is about 13%, the peak to Compton ratio is around 40.

Electronics

The output from a gamma-ray detector is, in essence, an amount of electrical charge proportional to the amount of gamma-ray energy absorbed by the detector. The function of the electronic system is to collect that charge, measure the amount, and store the information.

A typical simple electronic system for gamma-ray spectrometry is shown in Figure 3-1. The bias supply provides the electric field to sweep the electron-hole pairs out of the detector which are then collected by the preamplifier. The collected charge is then converted to a voltage pulse. The linear amplifier changes the pulse shape and increases its size. The multichannel analyzer (MCA) sorts the pulses by pulse height

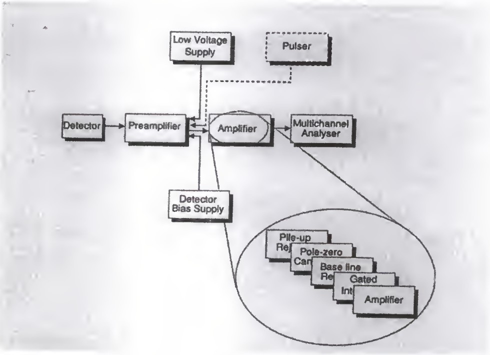

Figure 3-1. A schematic electronic system for gamma spectroscopy.

and counts the number of pulses within individual pulse height intervals. In modern systems the detector and the preamplifier are manufactured as a single unit, the first stage of the preamplifier being intimately attached to the detector capsule. This arrangement has advantages in that critical components of the preamplifier can be cooled to reduce thermal noise. More often the other items in the system that includes the MCA are purchased in the Nuclear Instrumentation Module (NIM) modular format. NIM modules are manufactured to standard physical dimensions and fit into a "slot" in a NIM-bin which contains standard electrical power supplies. The NIM standard also defines the pulse and logic specifications for the signals passing between modules. In this way, it is possible to install a variety of modules from different manufacturers within the same bin and for them to work together as part of a complete system.

The amplifier is a sophisticated part of the system. Its main function is pulse shaping, while amplification becomes an incidental function. An amplifier for high-resolution spectrometry must provide pole-zero cancellation, baseline restoration and pile-up rejection.

A NIM bin (model 4001A) from EG&G Ortec was used to accommodate the power supply (model 459) for the detector, amplifier (model 671), and spectrum master (MCA, model 919). Pulses from the detector were amplified and shaped with 2 microseconds differentiating time constant and applied to a 16834-channel pulse-height analyzer (multi-channel analyzer, MCA). Calibrations of pulse height versus photon energy for the spectrometer were performed using ^{241}Am, ^{137}Cs, and ^{60}Co. The curve was linear in the range from 10 keV to 2.0 MeV and to an accuracy of better than 1%. Pulse pileup rejection, baseline restorer, and pulse shaping function were adjusted to optimize the operating condition of the spectrometer.

Experimental setup

The detecting system employed in this experiment is show schematically in Figure 3-2.

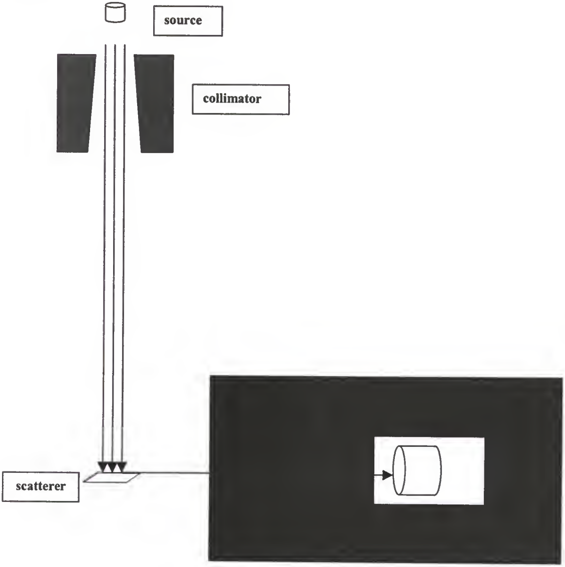

Figure 3-2. The experimental setup of incoherent scattering method (not to scale).

The HPGe detector first is placed at about 30 cm and then at 150 cm away from the beam axis of the cobalt-60 unit. The lead shielding surrounding the HPGe detector is at least 10.0 cm thick on the top and both sides. The lead shielding is 5.0 cm thick underneath the detector. The whole setup is mounted on a rigid frame. Radiation is admitted to the crystal through a lead collimator 20.0 cm long with a pinhole in the middle which has a radius of about 0.25 cm. Carbon is chosen as the scatterer based on the fact that the Compton cross section at this energy is predominant. The carbon scatterer is suspended at the isocenter of the machine; the collimator, and the detector, are optically aligned with the center of the scatter so the detector forms a 90° angle with the axis of the radiation beam from the cobalt-60 unit.

Measurement of spectra

A calibration curve, relating base line voltage on the MCA to photon energy, was obtained, using ^{241}Am (59.5 keV) and ^{137}Cs (661.6 keV) with the apparatus aligned and the gain of the amplifier suitably adjusted. With the scatterer in place, the cobalt-60 machine is then switched on, and a sufficient counting time (1800 sec) is taken to ensure reasonable statistical accuracy. The scatterer is then removed from the beam and a background run is taken using the same time intervals as before. The stability of the counting system is checked and with a drift of less than 1 keV. The difference between the two runs gives the scattered spectrum.

Two points should be noted. First the scattering angle 90° which is set as described above refers strictly to radiation coming from the center of the cobalt-60 source. Degraded radiation arising from the collimating system and reaching the detector will, in general, have undergone scattering through some angle different from 90°. Since the analysis of the data treats all photons as though they had been scattered through the same angle, the portion of the final (primary) spectrum due to radiation from the collimator will be a somewhat broadened or "smeared-out" version of the true spectrum.

Second, even though the background from the machine head and room scatter is subtracted, the background caused by the interactions between the scattered beam itself and the lead shielding material is always present. This can be minimized by optimal shielding design. Characteristic x rays will be present no matter how well the shielding is designed. Fortunately, they are easily distinguishable and can hardly pose a serious problem.

Effect of Collimator

The same detector and the associated electronics were used. The collimator was made of lead, with a pinhole of radius about 0.25 cm. The length of the collimator was about 20.0 cm. The ^{60}Co and ^{137}Cs calibration sources were placed 30 cm away from the detector. The spectra were measured with a counting time about 1800 seconds. The collimator was then put in between, and the spectra were measured again under the same conditions. All the spectra were then subtracted with corresponding backgrounds to determine the effect of the lead collimator.

CHAPTER 4
RESULTS AND DISCUSSION

Scattered Spectra

The once-scattered spectrum is measured with the minimum field size attainable, namely 5 by 5 cm at 100 cm to minimize the contributions from the cobalt-60 machine head. The spectrum obtained at an angle of 90^o and with background subtracted is shown in Figure 4-1.

We can see clearly the two scattered peaks from 1.173 MeV and 1.332 MeV along with an obvious continuum. This continuum is due to three factors: (a) contributions from the cobalt-60 machine head, (b) response function of the detector, including Compton edges and back-scattered peaks, and (c) photons escaping from the edge of the aperture of the collimator, including degraded photons, bremsstrahlung photons, and characteristic x-rays. Part (c) can be minimized by optimal design of the collimator. Part (b) can be eliminated theoretically by employing the so-called iterative unfolding technique (Sam D. 1968). The two scattered peaks from ^{60}Co are located at 356 keV and 369 keV and the full width at half maximum (FWHM) of these two scattered peaks are 4.8 keV and 4.7 keV, respectively. The line broadening of the of the scattered peaks is due to several factors. One is the finite size of the cobalt-60 source and the size of the scatterer, which makes the scattering angle not strictly 90^o.

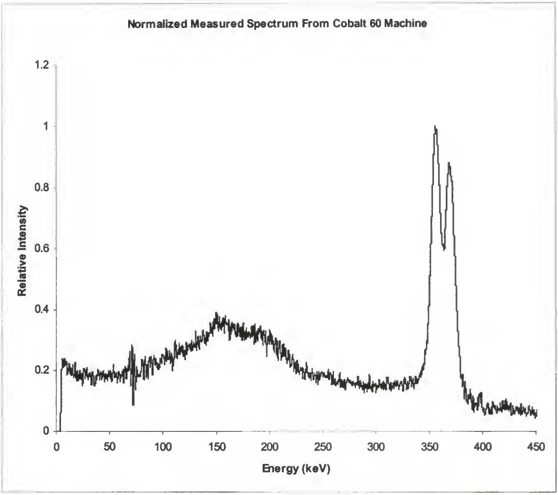

Figure 4-1. Measured scattered spectrum from cobalt-60 machine.

This is estimated to be 4.3 keV and is believed to contribute most to the line broadening. The second factor is the finite angle of acceptance, due to the aperture of the lead collimator, which also slightly changes the scattering angle. The aperture of the collimator is 0.5 cm in diameter, the distance from the scatterer to the aperture is 150 cm, the acceptance angle is about 0.3°, and its contribution to the line width is around 1.0 keV. The third factor is the intrinsic resolution of the spectrometer. This factor is approximately 1.6 keV. The quadratic summation of these three factors yields good agreement with the experimental data.

The original spectrum is reconstructed using the Compton energy-angle relation and the Klein-Nishina formula. The reconstructed original spectrum is shown in Figure 4-2. The FWHM of the corresponding two peaks is 52.8 keV and 61.1 keV.

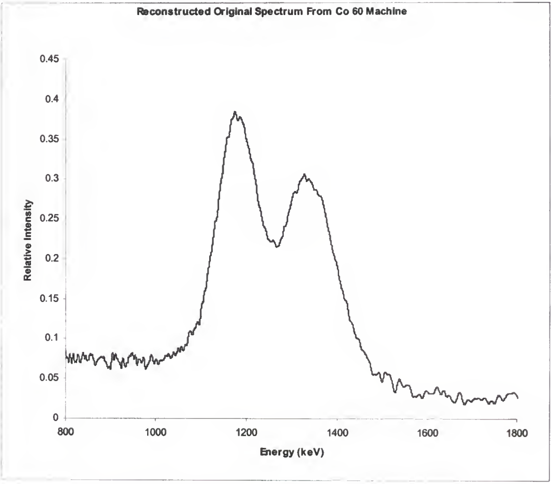

Figure 4-2. The reconstructed spectrum from the measured scattered spectrum (only two peaks) are shown.

Compared with a cobalt-60 spectrum directly measured, shown in Figure 4-3, the line width is significantly broadened.

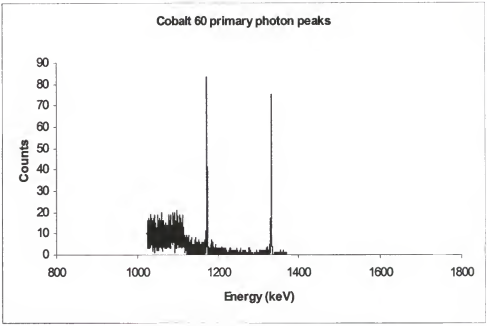

Figure 4-3. Primary photon peaks from ^{60}Co isotope.

In order to describe this line broadening effect, a " broadening factor" is introduced. This factor is given by dE_o/dE . Thus, if the FWHM of a Compton scattered peak is ΔE, the width of the corresponding line in the reconstructed original peak is given by:

$$\Delta E_o = \frac{dE_o}{dE}\Delta E = \left(1+\frac{E_o}{m_o c^2}(1-\cos\theta)\right)^2 \Delta E = \left(\frac{E_o}{E}\right)^2 \Delta E.$$

(4-1)

In the case of cobalt-60, for example, the lower energy gamma is 1172 keV and the 90° scattered energy is 356 keV. These values yield a broadening factor of

$$\left(\frac{E_o}{E}\right)^2 = \left(\frac{1172}{356}\right)^2 \cong 11$$

Since the FWHM of the 356 keV line in the scattered spectrum is about 4.8 keV, the FWHM of the reconstructed 1172 keV line in the original spectrum should be 53 keV. This unavoidable broadening effect of the reconstructed original spectrum is a direct consequence of the conservation of energy and momentum in the collision. This effect is a function of both incident photon energy and scattering angle. At a given scattering angle, the higher the incident photon energy, the more severe the broadening effect. At given incident photon energy, the larger the scattering angle, the more severe the broadening effect.

Effect of Collimator

The spectra of ^{60}Co and ^{137}Cs calibration sources with and without collimator are shown in Figure 4-4, Figure 4-5, Figure 4-6, and Figure 4-7. It can be seen that the collimator reduced the counts for the peaks and added to the continuum. The

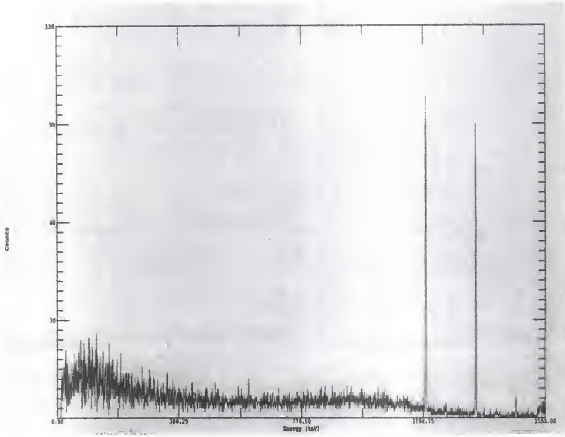

Figure 4-4. ^{60}Co spectrum with lead shielding.

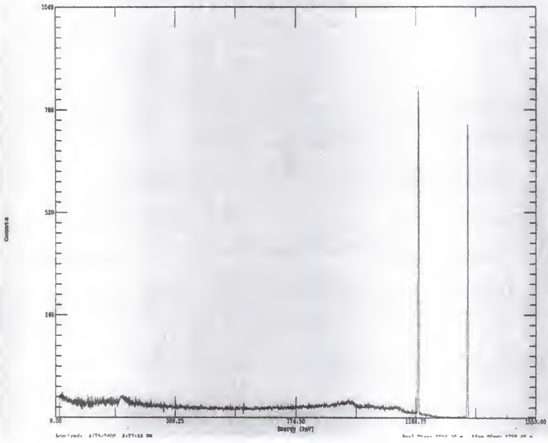

Figure 4-5. ^{60}Co spectrum without lead shielding.

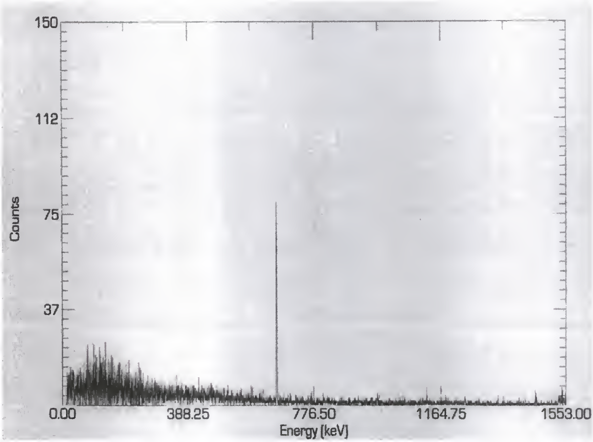

Figure 4-6. ^{137}Cs spectrum with lead shielding.

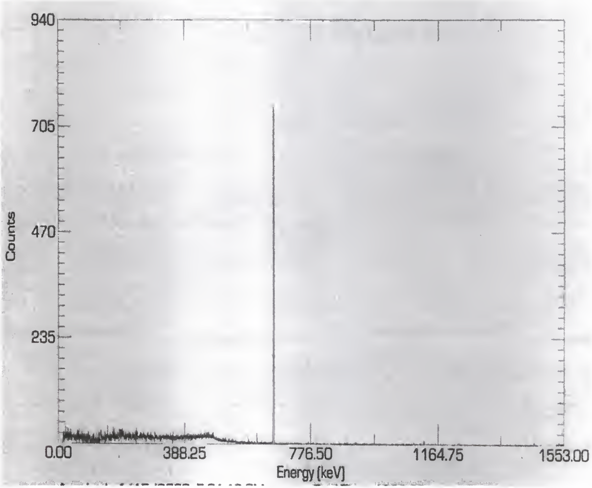

Figure 4-7. ^{137}Cs spectrum without lead shielding.

continuum is the cumulative contribution from incoherently scattered photons, characteristic x rays, and bremsstrahlung photons from the collimator. Even though the effect of the collimator can be observed rather easily and the correction of this effect can be effectively achieved, its theoretical treatment is difficult and one has to resort to the Monte Carlo technique if accurate correction is to be obtained.

CHAPTER 5
MONTE CARLO SIMULATION

The Monte Carlo simulation technique has found widespread application in the radiological sciences (Mackie 1990 and Andreo 1991). Monte Carlo simulation of photon beam transport has proven to be a valuable tool to determine and optimize the accuracy and the effectiveness of experimental measurements; it can also provide information which is otherwise inaccessible.

Our simulations were performed by means of the Monte Carlo code MCNP (Monte Carlo N-Particles, version 4B) (Briesmeister 1997). The code allows one to transport photons (in the energy range from 1 keV up to 100 MeV), neutrons (between 10^{-11} and 20 MeV), and electrons (between 1 keV and 100 MeV) through matter. For photons, MCNP has two interaction models: simple and detailed. The simple physics treatment ignores coherent (Thomson) scattering and fluorescent photons from photoelectric absorption. It is intended for high energy photon problems or problems where electrons are free and is also important for next event estimator such as point detectors, where scattering can be nearly straight ahead with coherent scatter. The detailed physics treatment includes coherent scattering and accounts for fluorescent photon after photoelectric absorption. Atomic form factors are used to account for electron binding effects. The detailed physics treatment is almost always used by default. It is the best treatment for most applications, particularly for high Z nuclides or deep penetration problems.

The generation of electrons from photons is handled in one of three ways. These three ways are the same for both the simple and detailed photon physics treatments. (1) If electron transport is turned on (Mode P E), then all photon collisions except coherent scatter that can create electrons are banked for later transport. (2) If electron transport is turned off (no E on the Mode card), then a thick-target bremsstrahlung (TTB) model is used. This model generates electrons, but assumes that they travel in the direction of the incident photon and that they are immediately annihilated. Any bremsstrahlung photons produced by the non-transported electrons are then banked for later transport. Thus, electron-induced photons are not neglected, but the expensive electron transport step is omitted. (3) If IDES=1 on the PHYS:P card, then all electron production is turned off, no electron-induced photons are created, and all electron energy is assumed to be locally deposited. The TTB approximation cannot be used in Mode P E problems, but it is the default for Mode P problems.

To use the MCNP code, the user must create an input file containing pertinent information to define the geometry, the source, and the materials. The code also offers a variety of tallies with which the concerned interactions can be scored. The variance reduction techniques offered by MCNP reduce the error and the calculation time.

Scattered Spectrum of Cobalt-60 Beam Simulation

The first simulation is a simple case where the scatterer is impinged by a point beam with photons of energy 1.172 and 1.332 MeV. The geometry is shown below in Figure 5-1. The cobalt-60 source is simulated as a cylinder with a radius of 1.0 cm and a height of 2.0 cm. The Ge detector is a ring with an inner radius of 30.0 cm and a outer radius of 35.0 cm. The detector is put behind a lead collimator which consists of a upper ring and a lower ring. Both lead rings have a inner radius of 10.0 cm and outer radius of 30.0 cm. The distance between the two lead rings is 0.5 cm, which

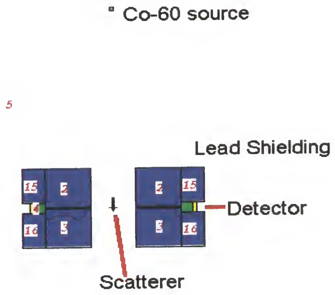

Figure 5-1. MCNP simulation geometry for point beam and size beam (The numbers in the figure denote different cells as defined by the MCNP code).

makes the collimator pinhole radius 0.25 cm. The carbon scatterer is a cylinder with a radius of 0.25 cm and a height of 1.0 cm. The spectrum result is shown in Figure 5-2. The calculation shows two clear 90° scattered peaks located at 356 and 369 keV. The Compton continuum and edge is very low due to the adequate size of the Ge detector. The broadening of the peaks is due to the finite solid angle and the finite thickness of the scatterer. Thus, the scattering angle is a small spread centered on 90°. This effect contributes to FWHM of about 4 keV.

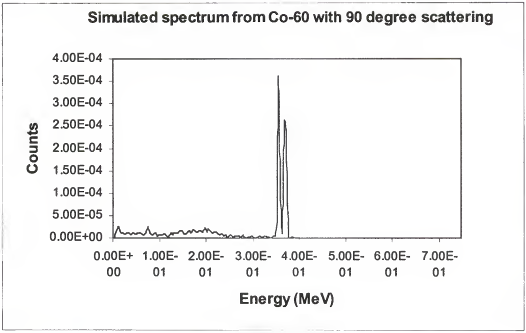

Figure 5-2. Simulated spectrum from cobalt-60 machine with 90° scattering (point beam case, uncertainty less than 10%).

In the second simulation, the beam is from a cobalt-60 cylinder with a radius of 1.0 cm and height 2.0 cm. The spectrum result is shown in Figure 5-3. In this case the finite size of the source is accounted for in addition to the effect mentioned above.

The spectrum shows a higher counting between 356 and 369 keV, the Compton continuum is also higher, and the Compton edge is not only higher but also broader due to greater spread of the spectrum.

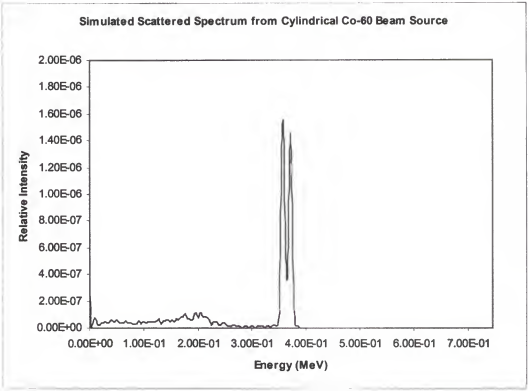

Figure 5-3. Simulated spectrum from cobalt-60 machine with 90° scattering (size beam case, uncertainty less than 10%).

Modeling of Cobalt-60 Machine

The spectrum from the cobalt-60 machine is a continuous spectrum, consisting of predominantly 1.172 MeV and 1.333 MeV photons with degraded photons from beam defining systems. The Theratron 1000 model cobalt-60 machine is a complicated electromechanical device. Particular attention has been paid to the careful modeling of the geometry and the material construction of three of its main components: the cobalt-60 source capsule, the source housing, and the collimator assembly. Although simplified in the modeling process, the most important features of each of these components have been retained. Figure 5-4 shows a drawing of the source capsule.

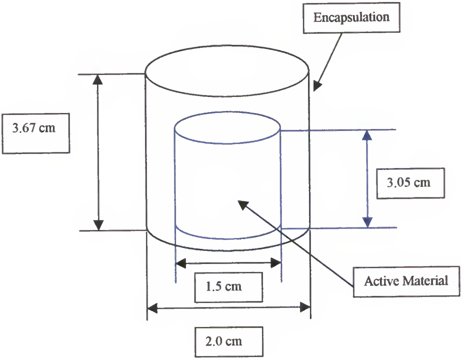

Figure 5-4. Source capsule design of Theratron 1000 cobalt-60 therapy machine.

Previous simulation shows that the nickel plating of the pellets has little effect on the spectrum, so the active material is modeled as homogeneous cobalt-60. In our MCNP simulation, we have used a value 1.0 cm for the diameter of the cobalt-60 active material region and a nominal value of 2.05 cm for its height. All the rest are modeled quite accurately according to the parameters given.

The primary definer is a fixed opening made of tungsten. The adjustable collimator made of intermeshing tungsten jaws is modeled as a continuous slab for the sake of computational simplicity. The trimmer bars are slightly curved, and are modeled as flat.

Primary Spectrum Simulation of Cobalt-60 Machine

For primary spectrum simulation, it is noted that cylindrical symmetry exists, which is to the advantage of the simulation. The scoring cell is placed beneath the machine; the distance between the cobalt-60 source and the scoring cell is 100 cm. MCNP tally type 4 (photon flux) F4 is used. The simulated primary spectrum is shown in Figure 5-5.

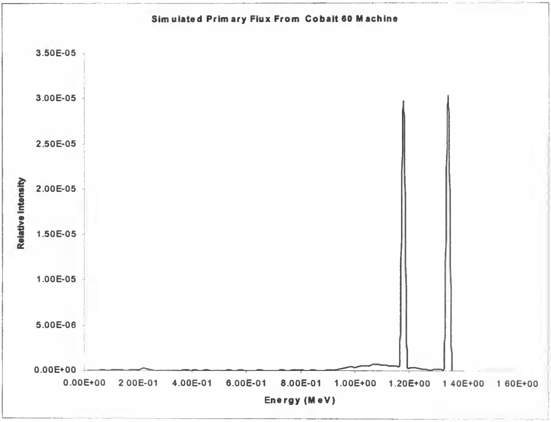

Figure 5-5. Simulated primary spectrum from cobalt-60 machine (uncertainty less than 10%).

Scattered Spectrum Simulation of Cobalt-60 Machine

The 90° scattered spectrum simulation can be a little difficult. The carbon scatterer is small, so the probability for photons to be 90°-scattered then enter the detector is very low. In addition, an MCNP tally type 8 (pulse height) F8 tally is needed to calculate the energy deposition in the Ge detector. This process is a purely analytical one, so no variance techniques are allowed in the simulation. This means that to obtain a spectrum with acceptable statistical deviation, protracted CPU time is needed. To circumvent these difficulties, the focus was shifted to obtain the flux entering a void cell that has the same volume as the detector. The resulting flux is input into a Ge detector with the same geometry to get the spectrum. When using MCNP to get flux tallies, various variance reduction techniques can be used. Those techniques include biasing the carbon scatterer's importance using the IMP:P card, employing forced collisions using the FCL:P card , and using a DXTRAN sphere. This DXTRAN sphere is positioned so that its center is in the void scoring cell. An additional card, DXC:P, is used to force the scattered photons from carbon to reach this scoring cell with an appropriately adjusted weight. Even in this way, about 10^9 particles have to be transported, which still requires several days for a typical calculation run by a ULTRA SPARC workstation.

The measurement experiment setup and the measured spectrum are both verified with an MCNP run with the detailed modeling of the machine head and the experiment setup. The whole model is shown in Figure 5-6. The simulation result is shown in Figure 5-7.

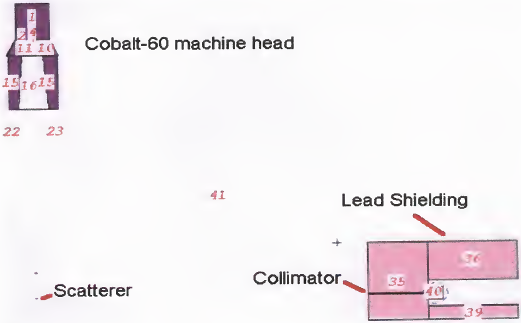

Figure 5-6. The actual MCNP geometry of the cobalt-60 machine head and the measurement setup (numbers indicate different cells as defined by the MCNP code).

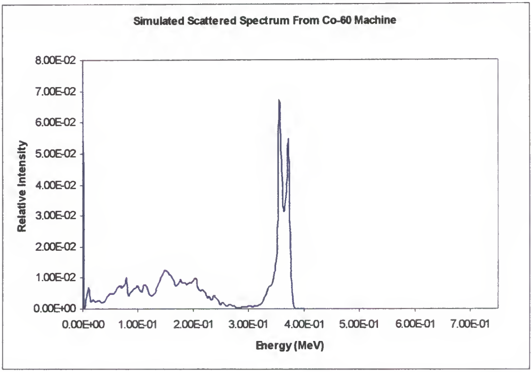

Figure 5-7. The actual simulation of the cobalt-60 machine with 90° scattering (uncertainty less than 10%).

Compared with the measured spectrum (Figure 4-1), excellent agreement in the peaks region is observed. However, lower continuum is observed from the simulation. This leads to the consideration of the effect of the lead collimator.

Effect of the Collimator

As observed above, the contribution from the collimator might be significant. To determine this effect qualitatively, a series of Monte Carlo simulations is done with a copper collimator whose pinhole radius is varied from 0 to 0.6 cm. The Ge crystal is 2.5 cm in radius and 5.0 cm in height. MCNP tally type 8 (F8, detector pulse height) is used. The simulated spectra for the copper collimator with different pinhole radii are shown in Figure 5-8. The simulated spectra for a 5.0 cm thick lead collimator with different pinhole radii are shown in Figure 5-9.

It is important to note that the distortion increases rapidly when the aperture size is reduced and the collimator thickness remains constant. The copper collimator distorts the spectrum more than does the lead collimator. This is because, in this energy range, copper scatters more and thus absorbs less while lead scatters less and absorbs more. This can be seen clearly from their photon cross sections table. The photon cross sections for copper and lead are shown in Figure 5-10 and Figure 5-11, respectively. The preferred mode of interaction to reduce the interference is photoelectric absorption. It is clearly shown that for lead the cross section for photoelectric absorption is larger than the incoherent scattering cross section beginning at 400 keV, while for copper this is not true until 120 keV.

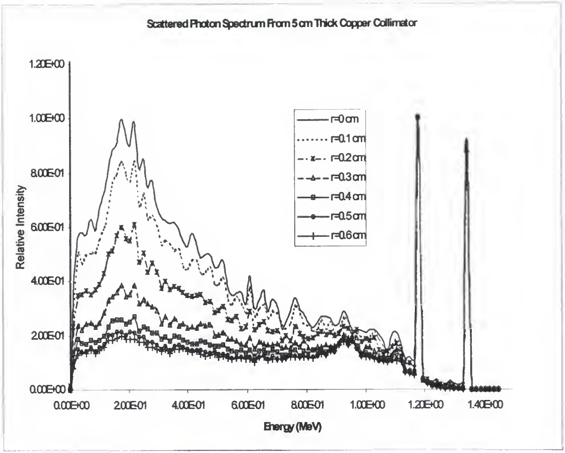

Figure 5-8. MNCP simulated spectra from ^{60}Co with 5.0 cm thick copper collimator, r is the radius of the pinhole of the collimator (uncertainty less than 1.0%).

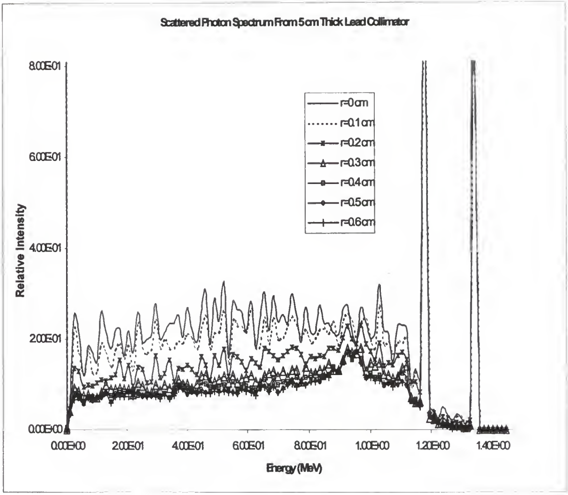

Figure 5-9. Simulated spectra from ^{60}Co with 5.0 cm thick lead collimator, r is the radius of the pinhole of the lead collimator (uncertainty less than 1.0%).

This means that after a scattering event, if the energy of the scattered photon is below 400 keV in lead, it most probably will be absorbed, while the energy of scattered photons in copper have to be below 120 keV for copper to do the same. In copper, photons have to undergo more scattering events to be reduced in energy and be absorbed. In this sense, lead possesses better radiological properties as a shielding material.

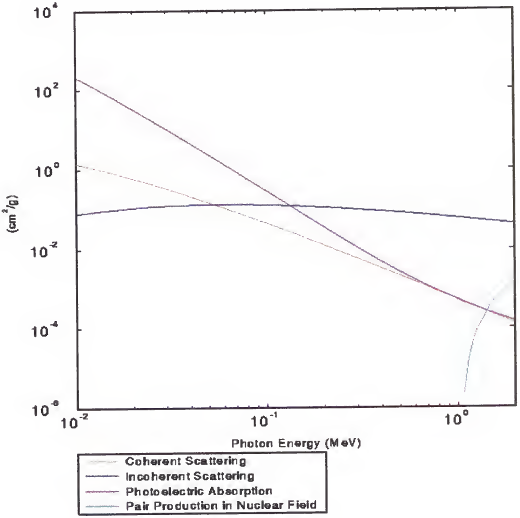

Figure 5-10. Photon cross sections for copper in the energy range of 10 keV–2MeV.

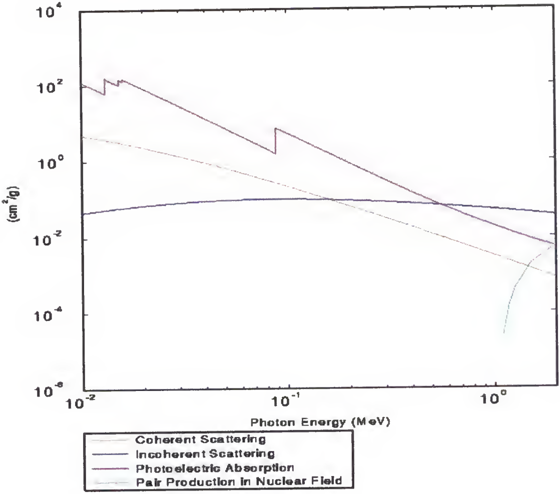

Figure 5-11. Photon cross section for lead in the energy range of 10 keV-2 MeV.

In addition, a spectrum from ^{60}Co is simulated with a lead collimator the thickness of which is 20.0 cm and pinhole radius is 0.6 cm. The spectrum is shown in Figure 5-12.

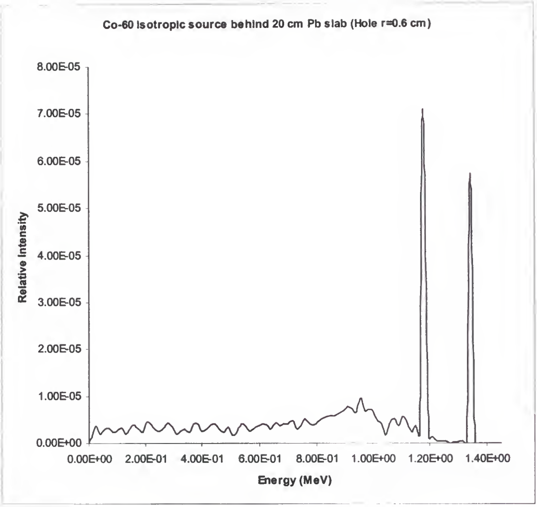

Figure 5-12. Simulate spectrum from ^{60}Co with 20.0 cm lead collimator, r=0.6 cm (uncertainty less than 1.0%).

Comparison with the spectrum in Figure 5-9 with the same pinhole size shows that a 5.0 cm thickness is not enough to minimize complication from the collimator. Compared with a ^{60}Co spectrum with no collimator (Figure5-5), we see that even a 20.0 cm thick lead collimator is not adequate if an accurate spectrum is to be measured. However, the increase in collimator thickness will increase the difficulty in the alignment between the scattered beam, the collimator aperture, and the detector.

Accurate alignment is important in this kind of measurement; otherwise the x-ray beam is incident obliquely on the collimator and penetrates through the edge of the aperture, thus causing considerable distortion of the measured spectrum.

CHAPTER 6
APPLICATION TO MEDICAL ELECTRON ACCELERATOR

Description of Medical Linear Accelerator

Medical electron accelerators can be found in virtually all radiation oncology departments. Their energy spectra are quantities of great importance. Many accelerators provide multiple electron and photon energies. The photon generating process in these electron accelerators is bremsstrahlung. When a beam of electrons impinges a target, usually made of high Z materials, the incident electrons interact with the target nuclei via inelastic scattering (kinetic energy of the interacting particles is not conserved in the interaction). The loss of kinetic energy is expressed as energy released as electromagnetic radiation during the interaction. A bremsstrahlung photon may possess an energy up to the entire kinetic energy of the incident electron. For low energy electrons, bremsstrahlung photons are released predominantly at right angles to the direction of the electrons. The angle decreases for electrons of higher energy. The probability of bremsstrahlung production increases with Z^2 of the target. The ratio of energy loss due to bremsstrahlung to that lost by excitation and ionization is approximately $E_k Z/820$, where E_k is the kinetic energy of the incident electrons in MeV, and Z is the atomic number of the target. Modern medical electron accelerators consist of several major components. These components produce the electrical power required to generate microwaves, conduct the microwave power to the accelerator wave-guide, and transport the beam to the patient.

There are four major components.

(1) The Modulator and Pulse-Forming Network

Medical electron accelerators require fairly large amount of electrical power. The power must be provided in pulses because accelerators accelerate particles in bursts. The modulator consists of a power supply that converts the incoming alternating current into direct current and the pulse-forming network that modulates the current into pulses. The pulses then are conducted to a magnetron or a klystron. The resulting microwave pulses are similar in shape to the electrical pulses, about several microseconds long and consisting of several MWs of power.

(2) The Magnetron and Klystron

Magnetron and Klystron are microwave-producing tubes where DC power is transformed into radio frequency power. A magnetron is a self-oscillator. It is kept tuned to the natural frequency of the accelerator structure by feedback (automatic frequency control, AFC) of a radio-frequency signal from the accelerator structure electromagnetic field to a motorized plunger in the magnetron cavity array. Magnetrons are commonly used in lower energy linear accelerators. The conversion efficiency can be as high as 60%. A typical magnetron provides 2 MW peak power. A klystron, on the other hand, is used as an amplifier and is used for high energy linear accelerators. Its frequency is determined by that of the radio-frequency driver. Its conversion efficiency can be up to 55%, with peak power as high as 24 MW.

(3) Microwave Power-Handling Equipment

Modern medical electron accelerators are multi-modal, capable of producing beams of electrons as well as one or more beams of x rays. Multi-modality accelerators require the microwave power delivered to the accelerator structure be modified, in order to accelerate particles to different energies. An energy switch is employed to control the amount of radio frequency power to be passed on.

(4) Treatment Head

This part is where photons are generated, the photon beam defined, and the dose monitored. It consists of a bending magnet, x-ray target, flattening filter, scattering foil, monitor ionization chamber, and collimator. The characteristics of the x-ray treatment beams are strongly influenced by the design of the treatment head. The desire for larger field sizes, improved beam characteristics, and convenient, functional accessories has led to a number of studies and improvements in treatment head design. The trend from lower- to higher-energy x-ray treatment beams, larger field sizes and the increasing use of accessories have resulted in an increase in treatment head size in terms of its height above the accelerator structure axis (radially away from isocenter) and its diameter below it. The former stems from the incorporation of the larger 270° bending magnet, thereby increasing the height of both the treatment head and the isocenter. The increase in diameter stems primarily from the requirement for large fields. Large, heavy, movable collimator jaws are needed for megavoltage x-ray beams with field sizes variable from zero area to as much as 40 by 40 cm^2 at 100 cm from the source. High-energy isocentric machines incorporate large bending magnets. These must be shielded extensively to attenuate radiation arising from their energy selection slits and elsewhere. A high-density, high atomic number material such as uranium, tungsten, or lead is frequently used to conserve space and to rapidly attenuate x rays. When tungsten or lead is employed for collimators, head shielding, x-ray targets, or flattening filters above 10 MV, photonneutron production increases rapidly.

At higher energies, x-ray flatness becomes increasing sensitive to angular and spatial misalignment of the x-ray lobe with respect to the axis of the flattening filter. Such misalignments can result from small changes in beam energy but are less likely to do so for achromatic magnet systems which may incorporate narrow energy defining slits. They are more likely to result from mechanical strains which occur from the stress of gantry rotation, from beam stopper extension or retraction, or from temperature changes of mechanical and electronic components, as well as from the presence of nearby ferromagnetic materials. Beam energy stability of a few percentage points is required to ensure satisfactory constancy of symmetry in bent-beam linear accelerators. If the energy of the beam entering the bending magnet from the accelerator structure shifts, the primary effect is a reduction in output. A secondary effect is a change in beam symmetry in the radial plane, the sense of the change depending on which side of the current maximum the new distribution is centered.

Other aspects of the treatment head involves the ionization chambers, the dosimetric system ,and the beam steering system.

Measurement of Spectrum

The same experimental setup used for cobalt-60 unit measurement is used for the measurement of the spectrum of a Phillips SL series linear accelerator at the Shands Cancer Center at the University of Florida. If the operating energy of the linear accelerator is high, a significant number of neutrons will be produced by high-energy x-ray beams. For most relevant materials, the neutron production threshold occurs at 8-10 MeV, rises rapidly, and then plateaus above 20 MeV photon energy. The photoneutron cross sections for tungsten and lead are shown in Figure 6-1 and Figure 6-2, respectively.

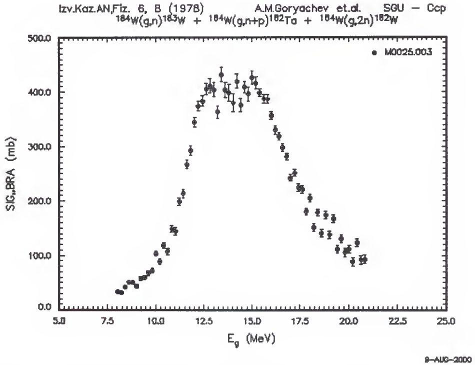

Figure 6-1. Photoneutron production cross sections for tungsten.

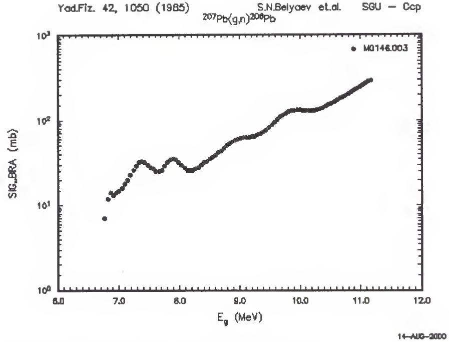

Figure 6-2. Photonneutron production cross sections in lead.

Neutrons that originate in the primary collimator, target, and flattening filter contaminate the photon beam. Others are filtered through the treatment head; some are generated in the patient and most are multiply scattered by barriers comprising the room. High-Z materials do not significantly alter the neutron fluence but do substantially reduce the average energy of the transmitted neutron spectrum. Depending on the material, energetic neutrons can induce radioactivity in the treatment head and patient support components, as well as in the treatment room barriers.

Neutrons will activate Ge, Cu, and Al in or around the HPGe detector when it is used to measure the photon spectrum from the linear accelerator, so neutron shielding is necessary in high energy cases. The neutron effect on the detecting system is shown in Figure 6-3. Some of the peaks are identified and are listed in Table 6-1.

Table 6-1. Peaks observed in neutron irradiated HPGe detector.

E (keV)	Origin
54	^{73m}Ge IT
67	^{73m}Ge IT
140	^{75m}Ge IT
175	^{71m}Ge
198	Summation ^{71m}Ge (22.7+175.2)
472	^{27}Al(n, alpha)
596	^{74}Ge(n, n')
609	^{74}Ge(n, n')
693	^{72}Ge(n, n')
868	^{73}Ge(n, gamma)
1698	^{27}Al(n, p,gamma)^{27}Mg
1779	^{27}Al(n, gamma)

Several attempts have been made to measure the spectra from medical linear accelerators. For a linear accelerator operating at 6 MeV at dose rate of 400 centi-grays per minute, the average beam current is about 100 mAs, pulse repetition frequency is around 300 pulses per second, and the pulse duration is 3.5 microseconds. Because the pulse shaping time of the amplifier in the detecting system is on the order of several microseconds, this means that in each beam burst of the machine, the detecting system can only pick up one or two photons. Given these constraints, obtaining a spectrum of acceptable statistics would mean the accelerator would have to operate for many hours, which will cause overheating. These

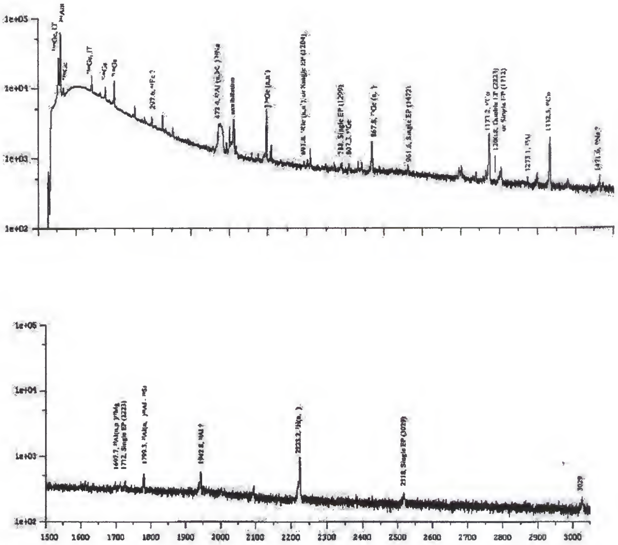

Figure 6-3. Neutron induced spectral characteristics of HPGe detector in the maze of a radiation therapy room with a linear accelerator operating at 20 MV.

accelerators are clinically calibrated, and we preferred not to adjust any of the operating parameters to keep the clinical conditions during measurement. Consequently, this severely hindered the efficiency of counting the spectrum. To remedy this situation, we needed a faster detector.

Monte Carlo Simulation

In order to fully understand the influence of the "broadening effect" on the spectra, the primary flux spectrum and the scattered flux spectrum from a medical linear accelerator are simulated with 90° scattering using the MCNP code. The simulation is an ideal case with no complication from the shielding, no generation of neutrons, and no response from the detector. The geometry of the MCNP simulation is shown in Figure 6-4.

The target assembly is composed of the target, primary collimator, and two flattening filters. The target is a tungsten/rhenium disk inset within a copper housing for cooling. The primary collimator is a 16.5 cm in diameter, 10.3 cm tall cylindrical tungsten piece with two 14.1 degree cones, symmetrically positioned about the center line. One cone is empty. It is used for all electron therapy modes and for low energy (LE = 6 MeV) photon therapy in conjunction with the LE flattening filter. The other cone is filled with a aluminum hardening filter and a HE flattening filter. It is used for high energy (HE = 20 MeV) photon therapy. For simplicity, only the high-energy photon cone is modeled and the primary collimator is chopped to a cylindrical

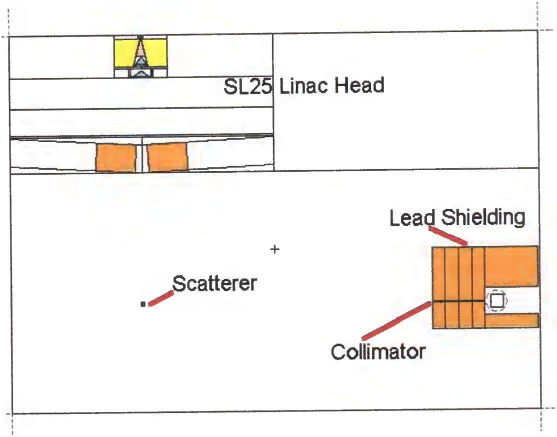

Figure 6-4. Geometry of MCNP simulation of SL25 Linac.

region just around the cone. The LE filter sits just below the primary collimator. The electron energy is a Gaussian distribution centered at 22 MeV. Electrons distribute uniformly within a spot size with a radius 0.05 cm (beam size). Two DXTRAN spheres are used at the positions of carbon scatterer and the detector to score sufficiently. The lead shielding is made to be a perfect absorber. The MCNP tallies are F2 (flux through a surface) and F4 (flux averaged over a cell).

The simulated primary flux spectra through the scatterer surface and in the scatterer are shown in Figure 6-5. The flux in the scatterer undergoes attenuation, so the intensity is lower except in the very low energy region where the intensity is higher. This is believed to be the result of scattering.

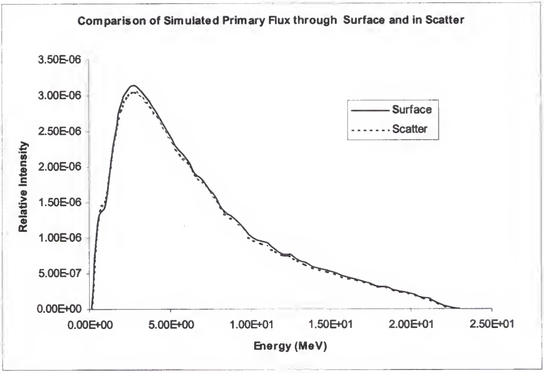

Figure 6-5. MCNP simulated primary flux spectra through the scatter surface and in the scatterer (uncertainty less than 1.0%).

The primary flux spectrum is transformed to a scattered flux spectrum using the Klein-Nishina formula; the result is shown in Figure 6-6. The MCNP simulated scattered flux spectrum is also shown in Figure 6-6 after energy bin adjustments and pair production correction. The general agreement between them is good except in the low energy region. The difference is that the MCNP simulated scattered flux spectrum has geometric broadening due to the pinhole size of the collimator. The theoretically predicted scattered flux spectrum is an ideal case, possessing no broadening effect.

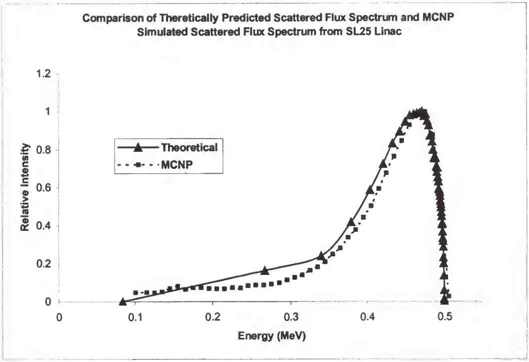

Figure 6-6. Comparison of theoretically predicted scattered flux spectrum from primary flux in the scatterer and MCNP simulated scattered flux spectrum (simulation uncertainty less than 1.0%).

The MCNP simulated scattered flux spectrum is used to reconstruct the primary flux spectrum. The result is shown in Figure 6-7. Again, the general agreement is good except in the low energy region. From this simulation, we can see, without all the complications (and line broadening effect minimized), this method can render good results. Unfortunately, in real experiments, neutron generation, detector response, shielding complication, and line broadening are always present. Some of the complications, like the neutrons and shielding complication can be minimized experimentally the effect, others, like the detector response, can be obtained only by complicated methods like the Monte Carlo technique because of the continuous

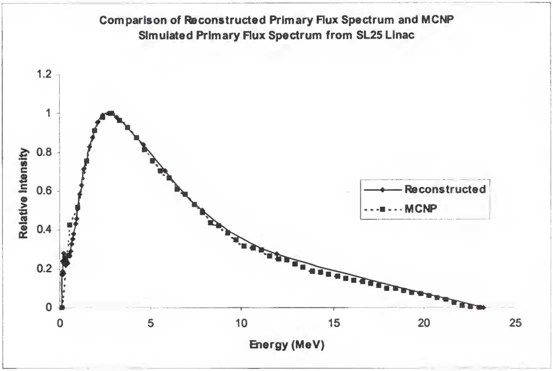

Figure 6-7. Comparison of reconstructed primary flux spectrum and MCNP simulated primary flux spectrum (uncertainty less than 1.0%).

nature of the spectrum. While the line broadening effect is a factor that again can be minimized by using smaller pinhole size, detecting efficiency will suffer, so the choice of the pinhole size is a compromise between detecting efficiency and resolution. This interconnection is shown in Figure 6-8 and Figure 6-9.

As we know, the relative resolution for current HPGe detector is about 0.1% (1.6 keV at 1.33 MeV, worse at higher energies). This is the resolution limit when HPGe is used to measure the scattered spectrum. As shown in Figure 6-8, for 20 MeV incident photons, after reconstruction, the resolution will deteriorate to about 4%.

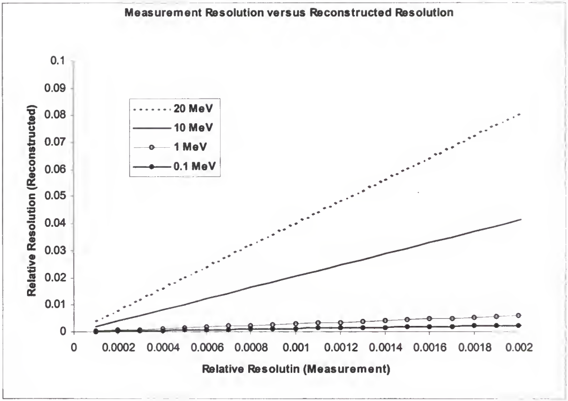

Figure 6-8. Measurement resolution versus reconstructed resolution with 90° scattering by different incident energy.

If the line broadening effect causes the measured scattered spectrum an additional 0.02% resolution loss, the total deterioration of the reconstructed spectrum will be about 5%. This effect is more severe as energy increases. As can be seen from Figure 6-9, it becomes severe when the scattering angle becomes large. Thus, in the high energy region and with a medium to large scattering angle, the reconstructed

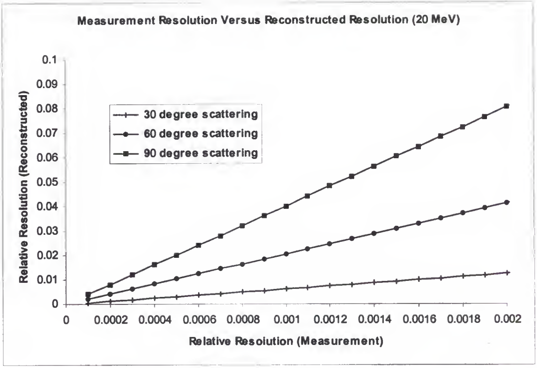

Figure 6-9. Measurement resolution versus reconstructed resolution for incident energy of 20 MeV with different scattering angles.

spectrum is very sensitive to resolution changes in the scattered spectrum. This imposes a limiting factor for current detector and associated electronics.

CHAPTER 7
CONCLUSIONS

In this research, several methods for obtaining spectral information from x-ray machines with different energy ranges have been reviewed. The advantages and limitations of incoherent scattering spectroscopy (ISS) method are discussed based on the review of other methods. The main advantage of the ISS method is the possibility of obtaining the spatial distribution information of photons by scanning the x-ray beam plane using a small target, scattering the primary beam to a collimated energy sensitive detector.

A complete set of analytical formulations for the incoherent scattering spectroscopy method has been developed. Detailed experimental and Monte Carlo simulations were carried out to fully evaluate the potential and limitations of the ISS method. The choice of scattering angle was evaluated considering the incident photon energy and the detecting efficiency of the detector. The choice of shielding material and the choice of scattering materials were assessed based on the radiation interaction properties of the materials. It has been found that for incoherent scattering purposes, low Z materials like carbon and beryllium are more suitable than high Z materials like lead and tungsten. For low Z materials, in most energy ranges, incoherent scattering process could be treated as Compton scattering where the energy-angular correlation provide a direct transformation from energy space to angular space.

The spatial and high-resolution spectral capabilities of the ISS method were evaluated using the cobalt-60 radiation therapy unit. A theoretical model for the energy broadening effect was developed and the cobalt-60 radiation therapy beam was used to validate the theory. The energy broadening effect systematically reduced the energy resolution of the spectra reconstructed from the scattered spectra measured by ISS method. Both the geometric line broadening and the FWHM of the detector contributed to this phenomenon. The effect became more severe at higher energies or at larger scattering angles due to the larger amount of energy loss under these situations. It was noted that the energy broadening effect had been consistently neglected in the past experimental approaches using low energy resolution NaI detectors.

Monte Carlo simulation using MCNP-4C were performed to assess the accuracy and precision of the ISS method. Experimental results form the cobalt-60 machine was used to benchmark and validate the MCNP-4C. The effect of the collimator was found to complicate the measurement in two ways. First, characteristic x rays and multiple scattered photons with degraded energies would enter the detector. Second, the size of the pinhole of the collimator would generate geometric broadening effect due to the inaccuracy in defining the scattering angle. The effect of the collimator was investigated using the Monte Carlo simulation technique. The severity of the first effect was dependent again on the radiation interaction properties of the shielding material.

A detailed MCNP-4C model was developed to obtain the primary and the scattered spectra from a medical linear accelerator. The theoretically predicted scattered spectrum and the MCNP-4C simulated scattered fluence spectrum were compared and good agreement was found. The MCNP-4C simulated scattered fluence spectrum was transformed back to the primary flux spectrum and good agreement again was found. These simulations confirmed the applicability of the method under ideal conditions, when no neutron generation, no detector response, and no complication from the shielding materials were present. It is thus concluded that in real experimental situations, where all these complications are present, the requirement for the detector becomes very high; the resolution, in particular, is found to be the limiting factor if accurate spectral information is to be obtained experimentally.

Based on results found in this research the following specific conclusions are made:

1. The incoherent scattering spectroscopy could be used to measure the spatial and spectral characteristics of high-energy x-rays beams.
2. The high spatial and energy resolution capabilities of the ISS method were demonstrated using a cobalt-60 radiation therapy beam.
3. The energy broadening effect due to the energy transformation during the scattering process and detector collimation geometry reduces the energy resolution of the ISS method.
4. A rigorous theoretical model for prediction and correction of the energy-broadening factor is developed.
5. Due to the extremely short duration of LINAC pulses and detector charge collection time, not more than a couple of photons per pulse could be

detected. This increases the length of the measurement time and severely limits the applicability of the ISS method to LINAC medical x-ray machines.

APPENDIX A
MCNP INPUT FILE FOR COBALT-60 MACHINE SIMULATION

```
Co-60 machine scattered flux spectrum simulation
C carbon importance is 5, forced collision is 1
C dxtran spheres defined at (32 0 -100) with radius 3 and 4 cm
C contribution to dxtran spheres from carbon scatter is 10, the rest are
C all zero. Direction is biased too.
C No electron transport, and the photon importance fro wooden boards,
C concrete floor and Lucite tube are not zero.
C Changed 11/18/99 from co5
C cell cards
1  1    -19.3    -1 -2  10       $W, thickness 10 cm above source
2  1    -19.3    5 -1 -10  6    $W, around the source
3  1    -19.3    -5  -10  9      $W, source upper cap
4  2     -7.8      -5  -9  8    $No.416 stainless steel, source middle part
5  2    -7.8      -5  4 -8  7  $No. 416, source wall around the active material
6  2    -7.8      -5  -7  6     $No.416, source bottom
7  3    -8.9      -4  -8  7      $Co and Ni, active material
c 10  1    -19.3  -11 -6  18    $W, primary definer
10  1   -19.3  -11 -6  18  #11   $W, primary definer
11  0         -6 18 -23 -24 -25 -26  $Hole in the definer
12  9   -0.92  12 -14 15 -16 -63 19  $Upper wooden board 2 cm
13  9   -0.92  12 -14 15 -16 -20 21  $lower wooden board 2 cm
14  10  -2.3   12 -14 15 -16 -21 22  $Concrete Floor 6 cm thick
c 15  1    -19.3  -27 28 -29 30 -31 -18 32  $W, leaves
15 1    -19.3   -27 -18 32  #16    $W, leaves
16 0          -28  -29 -30 -31 -18 32     $Square hole in leaves
20  1   -19.3  -33 34 -39 300 38 -37       $W, upper trimmer bar
21  1   -19.3  -33 34 -311 40 38 -37       $W, upper trimmer bar
22  1   -19.3  -35 36 38 -219 -39 40       $W, lower trimmer bar
23  1   -19.3  -35 36 218 -37 -39 40       $W, lower trimmer bar
25  4   -1.48  -41 42 -43 44 -45 46       $carbon sheet scatter
28  5   -1.19      50 -51 -52 53       $Lucite tube before lead collimator
c Cerrobend block with hole(diameter 0.5 cm) in the lucite tube
c the total length is 3.2 cm, 2 cm is inserted into lead collimator
30  6  -9.4  -50 55 54 -52  $cerrobend before lead collimator
c lead collimator and blocks before the detector
```

```
31  0         -55  64  -66 $Hole in lead collimator radius 0.25cm
32  0          -56 66 -67 $Hole in lead collimator  radius 0.5cm
33  0          -57 67 -68 $Hole in lead collimator  radius 1.0cm
34  0       -58  68  -65  $Hole in lead collimator  radius 1.5cm
35  7  -11.35  55 -60 61 -62 63 64 -66   $Pb
351  7  -11.35  56 -60 61 -62 63 66 -67   $Pb
352  7  -11.35  57 -60 61 -62 63 67 -68   $Pb
353  7  -11.35  58 -60 61 -62 63 68 -65   $Pb
c lead blocks above the detector
36 7  -11.35  -70 71 -74 76 78 -79
c lead blocks in the left of the detector
37 7  -11.35  -71 72  -74 75 78 -79
c lead blocks in the right of the detector
38  7 -11.35  -71 72  76 -77  78 -79
c lead blocks below the detector
39  7 -11.35  -72 73 -74 76 78 -79
c this is the void scoring cylinder
40  0       -80 78 -81 $void scoring cylinder
c this is void inside the cylinder with non zero importance
41   0 -85 -86  87  #1 #2 #3 #4 #5 #6 #7  &
       #10 #11 #12 #13 #14 #15 #16 #20 #21 #22 #23 &
       #25 #28 #30 #31 #32 #33 #34 &
       #35 #351 #352 #353 #36 #37 #38 #39 #40  $void
c This is the world
42   0        85:86:-87     $world

c surface cards
c The origin is chosen at the bottom of the source (where it is also
c the beginning of the primary definer).
1   cz     5.588                     $radius of the W upper shielding
2   pz     13.67
4   cz     1.0          $radius of the active material
5   cz     1.17         $radius of the source including the casing
6   pz     0.0          $bottom of the source
7   pz     0.11         $bottom stainless steel thickness
8   pz     2.16
9   pz     3.16
10  pz     3.67
11  kz     11.45   0.23816   $primary definer outer cone
c 11  kz      11.45   0.5    $primary definer outer cone1
12  px   -20
14  px   80
15  py   -25
16  py    25
```

```
c 13  pz     -3.175              $primary definer upper boundary
18  pz     -6.35                $primary definer lower boundary
19  pz      -112  $lower boundary of upper wooden board
20  pz     -130  $upper boundary of lower wooden board
21  pz     -132  $lower boudary of lower wooden board
22  pz     -138  $lower boudary of concrete floor
23  p    16.6256 0.0 4.5361 25.038
24  p    -16.6256 0.0 4.5361 25.038
25  p    0.0 16.6256 4.5361 25.038
26  p    0.0 -16.6256 4.5361 25.038
c 27  cz  3.294       $radius of the leaves
c 27  cz  4.294       $radius of the leaves
27  cz  8.294  $radius of the leaves
28  p  240 0.0  18.0 720
29  p  -240 0.0  18.0 720
30  p  0.0  240 18.0 720
31  p  0.0 -240 18.0 720
218  px   5
219  px  -5
300  py   5
311  py  -5
32  pz  -26.823
c the distance from the bottom of the leaf to the upper trimmer bar is 4 cm.
C The following surfaces describe the trimmer bars.
33  pz  -30.94
34  pz  -33.48
35  pz  -33.90
36  pz  -36.44
37  px   8.2686
38  px  -8.2686
39  py   8.2686
40  py  -8.2686
c the following surfaces describe the carbon scatter
41  pz  -100
42  pz  -100.1
43  px  0.25
44  px  -0.25
45  py   0.9
46  py  -0.9
c the following surfaces describe the Lucite tube
50 c/x  0 -100 0.95  $ inner radius
51 c/x  0 -100 1.25   $outer radius
52  px  9.3              $length of the tube without cerrobend
53  px  -0.25   $same as surface 44
54  px  7.3
```

```
55 c/x  0 -100 0.25    $ radius of hole in cerrobend
56 c/x  0 -100 0.5
57 c/x  0 -100 1.0
58 c/x  0 -100 1.5
c the following surfaces describe the lead collimator and blocks
60 py  10
61 py  -10
62 pz  -80
63 pz  -110
64 px   9.3  $same as surface 52
65 px   29.3
66 px   14.3
67 px   19.3
68 px   24.3
c the following surfaces describe the lead blocks above and around c the detector
70  pz   -80
71  pz   -95
72  pz   -105
73  pz   -110
74  py   10
75  py    5
76  py   -10
77  py   -5
78  px   29.3  $same as 65
79  px   89.3
c the following surfaces describe the Ge  detector
80  c/x   0  -100  2.5
81  px   34.3
c the following surfaces describe the world
85 cz  100
86 pz  20
87 pz  -140

c data cards
mode  p
imp:p  1 16r 1 5 1 13r 1 1 0  $carbon region biased
c imp:p 1 8r 0 0 0 1 5r 5 0 1 12r 1 1 0 $carbon region biased
c This is  a cylindrical isotropic source
sdef erg=d1 pos=0 0 1.13 cel=7  rad=d2 ext=d3 axs=0 0 1 dir=d4 vec=0 0 -1
si1 L 1.172  1.332
sp1 d  1.0 1.0
si2  0.0  1.0
si3  -1.025 1.025
si4 H -1 -0.866 0.866    1
sp4 D  0  1     0       1
```

```
f404:p   40
e404 0.01 79i 0.4
dxt:p  32 0 -100 3 4
dxc:p  0 16r 0 10 0 13r 0 0 0  $carbon contribution 10 to dxtran
fcl:p   0 16r 0 1  0 13r 0 0 0  $carbon region biased
prdmp  300000000  -800 1 2 0
m1     74000  1.0                $W
m2     26000  1.0                $Fe
m3     27060  1.0                $Co
m4     6000    1.0                $C
m5     1000  -0.0805  6000 -0.5999 8000  -0.3196  $Lucite
m6     83000 -0.5  82000 -0.267  50000 -0.133  48000  -0.1   $Cerrobend
m7     82000  1.0                $Pb
c m8     32000   1.0
m9     1000  -0.1196  6000 -0.6372 7000 -0.008 8000 -0.2323
       11000 -0.0005  15000 -0.0002 16000 -0.0007
       17000 -0.0012  19000 -0.0003 $Wood, using adipose fat data from Attix
m10    1000  -0.0056   8000 -0.4983 12000 -0.0024
       11000 -0.0171  13000 -0.0456 14000 -0.3158
       16000 -0.0012 19000 -0.0192 20000 -0.0826
       26000 -0.0122 $concrete, using data from Hubbel
nps  900000000
```

APPENDIX B
MCNP INPUT FILE FOR SL25 LINAC SIMULATION

```
Linac Spectra Simulation
c
c *********************
c  Problem Description
c *********************
c
c It is desired to determine the primary and 90
c degree scattered spectrum from SL25 linac
c   A 10x10 field size is used for calibration.
c
c *******************
c  Cell Descriptions
c *******************
c
c -------------------------------------
c  Target, Primary Collimator & Filters
c -------------------------------------
c  Owns cells 100-399 and surfaces 100-399.
c
c  The target assembly is composed of the target, primary
c  collimator and two flattening filters.  The target is a
c  tungsten/rhenium disk set inset within a copper housing
c  for cooling.  The primary collimator is a 16.5 cm
c  diameter, 10.3 cm tall cylindrical tungsten piece with
c  two 14.1 degree cones, symmetrically positioned about
c  the center line.  One cone is empty.  It is used for all
c  electron therapy modes and for low energy (LE = 6 MeV)
c  photon therapy in conjunction with the LE  flattening
c  filter.  The other cone is filled with an aluminum
c  hardening filter and a HE flattening filter.  It is
c  used for high energy (HE = 20 MeV) photon therapy.  For
c  simplicity, only the high energy photon cone is modeled
c  and the primary collimator is choped to a cylindrical
c  region just around the cone.  The LE filter sits just
c  below the primary collimator.
```

```
c
c Tungsten/Rhenium electron target
 101 11 -19.47      -101   202 -201
c
c Copper housing/cooling for electron target
 111 12  -8.96      -101   209 -202
 112 12  -8.96  101 -102   209 -201
c
c Air around target assembly
 199  0         102 -121   209 -201
c
c
c Primary (tungsten) collimator
 201 13 -18.78  311 -121   215 -209
c
c Aluminum hardening filter for 25 MeV photon mode
c   (within primary collimator)
 211 14  -2.7       -311   211 -209
c
c Air above and below flattening filter
c   (within primary collimator)
 291  0         312 -311   214 -211
 298  0         319 -313   215 -212
 299  0         319 -121   219 -215
c
c Flattening filter for 25 MeV photon mode
c   (within primary collimator)
 221 15  -7.9       -312   212
 222 15  -7.9       -319      -212
 223 15  -7.9   313 -312   215 -212
 224 15  -7.9   312 -311   215 -214
c
c
c Flattening filter for all photon modes
 301 15  -7.9       -321   233
 302 15  -7.9       -111   239 -233
 303 15  -7.9   111 -112   239 -231
 304 15  -7.9   112 -113   239 -232
c
c Air surrounding flattening filter
 391  0         321 -111   233 -219
 392  0         111 -112   231 -219
 393  0         112 -113   232 -219
 394  0         113 -121   239 -219
```

```
c
c  Air surrounding target and filters
 399  0              121    239  -201
               410  -412    420  -422
c
c -------------------------
c  Collimator Jaw Assembly
c -------------------------
c  Owns cells 400-499 and surfaces 400-499.
c
c
c  Positive Y collimator
 401  16  -11.35    -480  481    482 -483    484 -485
c
c  Air around positive Y collimator
 404  0         -239  480    411 -412    420 -422
 405  0         -481  400    411 -412    420 -422
 406  0         -480  481    411 -482    420 -422
 407  0         -480  481    483 -412    420 -422
 408  0         -480  481    482 -483    420 -484
 409  0         -480  481    482 -483    485 -422
c
c
c  Negative Y collimator
 411  16  -11.35    -490  491    -492  493    494 -495
c
c  Air around negative Y collimator
 414  0         -239 490     410 -411    420 -422
 415  0         -491 400     410 -411    420 -422
 416  0         -490 491     410 -493    420 -422
 417  0         -490 491     492 -411    420 -422
 418  0         -490 491     493 -492    420 -494
 419  0         -490 491     493 -492    495 -422
c
c
c  Positive X collimator
 421  16  -11.35    -460 461     462 -463    464 -465
c
c  Air around positive X collimator
 424  0         -400 460     410 -412    421 -422
 425  0         -461 401     410 -412    421 -422
 426  0         -460 461     410 -412    421 -464
 427  0         -460 461     410 -412    465 -422
 428  0         -460 461     410 -462    464 -465
 429  0         -460 461     463 -412    464 -465
```

```
c
c
c Negative X collimator
 431  16  -11.35    -470 471     472 -473   -474  475
c
c Air around negative X collimator
 434  0           -400 470     410 -412    420 -421
 435  0           -471 401     410 -412    420 -421
 436  0           -470 471     410 -412    420 -475
 437  0           -470 471     410 -412    474 -421
 438  0           -470 471     410 -472    475 -474
 439  0           -470 471     473 -412    475 -474
c
c --------------------
c Scatterer Assembly
c --------------------
c Owns cells 500-599 and surfaces 500-599.
c Carbon scatterer is 0.5 cm in radius and 1 cm long.
c
 501  17   -1.8    -501                  522 -521
 502  0           -511          ( 501:   521:-522 )
 509  0           -422 420     410 -412    634 -401    511
c
c -------------------
c Detector Assembly
c -------------------
c Owns cells 600-699 and surfaces 600-699.
c Flight path through lead shield has a radius of 0.25 cm.
c
 601  0           -612 611                        -601
 602  0                                       -602
c
 611  0           -611 422     621 -624    634 -631
 612  0           -615 612     622 -623    633 -632    602
c
 621  16  -11.35    -612 611     621 -624    634 -631    601
 622  16  -11.35    -615 612     621 -624    634 -631
             (           623:-622 :  632:-633 )
c
 633  0           -615 422     410 -412    634 -201
             (           624:-621 :  631      )
c
c ---------------
c Outside world
c ---------------
```

```
c
99999  0         -420:615 :  412:-410 :  201:-634
c
c ************************
c  END Cell Descriptions
c ************************
c

c
c ***********************
c  Surface Descriptions
c ***********************
c
c ----------------------------------------
c  Target, Primary Collimator & Filters
c ----------------------------------------
c  Surfaces 100-399.
c
  101  cz   0.2725
  102  cz   1.0
c
  111  cz   3.85
  112  cz   4.0
  113  cz   4.65
c
  121  cz  10.0
c
c
  201  pz  -0.0
  202  pz  -0.1
  209  pz  -1.5
c
  211  pz  -7.62
  212  pz -10.6
  214  pz -11.57
  215  pz -11.79
  219  pz -12.4
c
  231  pz -14.86
  232  pz -15.11
  233  pz -15.46
  239  pz -15.66
c
c
  311  kz  -1.028  0.0631       -1
```

```
 312  kz   -7.84   0.416          -1
 313  kz   -9.94   1.653          -1
 319  kz  -12.32   0.1914         +1
c
 321  kz  -13.26   1.83376736112  -1
c
c -------------------------
c  Collimator Jaw Assembly
c -------------------------
c  Surfaces 400-499.
c  Collimator opening set for a 10x10 field size
c
 400  pz  -38.0
 401  pz  -51.0
c
 410  py  -20.0
 411  py    0.0
 412  py   20.0
c
 420  px  -20.0
 421  px    0.0
 422  px   20.0
c
 460  p    -4.9937526E-02   0.0000000E+00   9.9875234E-01  -4.0800000E+01
 461  p    -4.9937526E-02   0.0000000E+00   9.9875234E-01  -5.0800000E+01
 462  py   -1.1000000E+01
 463  py    1.1000000E+01
 464  p     9.9875234E-01   0.0000000E+00   4.9937526E-02   1.0000000E-03
 465  p     9.9875234E-01   0.0000000E+00   4.9937526E-02   1.5001000E+01
c
 470  p     4.9937526E-02   0.0000000E+00   9.9875234E-01  -4.0800000E+01
 471  p     4.9937526E-02   0.0000000E+00   9.9875234E-01  -5.0800000E+01
 472  py   -1.1000000E+01
 473  py    1.1000000E+01
 474  p     9.9875234E-01   0.0000000E+00  -4.9937526E-02  -1.0000000E-03
 475  p     9.9875234E-01   0.0000000E+00  -4.9937526E-02  -1.5001000E+01
c
 480  p     0.0000000E+00  -4.9937526E-02   9.9875234E-01  -2.7100000E+01
 481  p     0.0000000E+00  -4.9937526E-02   9.9875234E-01  -3.7100000E+01
 482  p     0.0000000E+00   9.9875234E-01   4.9937526E-02   1.0000000E-03
 483  p     0.0000000E+00   9.9875234E-01   4.9937526E-02   1.5001000E+01
 484  px   -1.1000000E+01
 485  px    1.1000000E+01
c
 490  p     0.0000000E+00   4.9937526E-02   9.9875234E-01  -2.7100000E+01
 491 p   0.0000000E+00  4.9937526E-02  9.9875234E-01  -3.7100000E+01
 492 p   0.0000000E+00  9.9875234E-01  -4.9937526E-02  -1.0000000E-03
 493 p   0.0000000E+00  9.9875234E-01  -4.9937526E-02  -1.5001000E+01
 494 px  -1.1000000E+01
 495 px   1.1000000E+01
c
c -------------------
c  Scatterer Assembly
c -------------------
c  Surfaces 500-599.
c
c These are surfaces for Carbon scatter
 501  cz   0.5
c
 511  sz -100.0  0.71
c
 521  pz  -99.5
 522  pz -100.5
c
c ------------------
c  Detector Assembly
c ------------------
c  Surfaces 600-699.
c
 601 c/x   0.0  -100.0    0.25
 602   s  133.8    0.0  -100.0  0.25
c
 611  px  109.3
 612  px  129.3
 613  px  131.3
 614  px  136.3
 615  px  149.3
c
 621  py  -10.0
 622  py   -5.0
 623  py    5.0
 624  py   10.0
c
 631  pz  -80.0
 632  pz  -95.0
 633  pz -105.0
 634  pz -110.0
c
c **************************
c  END Surface Descriptions
```

```
c **************************
c

c
c ***********************
c  Material Descriptions
c ***********************
c
c   ------------------------
c   Tungsten / Rhenium Target
c   ------------------------
c   Density of 19.47 grams per cubic centimeter.
c
c   The target is tungsten alloyed with 10 w/o rhenium.
c
m11    plib=02p  elib=03e
      74000  -0.9
      75000  -0.1
c
c   -------------------------------
c   Copper Support/Cooling Structure
c   -------------------------------
c   Density of 8.96 grams per cubic centimeter.
c
m12    plib=02p  elib=03e
      29000   1
c
c   ------------------------
c   Tungsten Alloy Collimator
c   ------------------------
c   Density of 18.78 grams per cubic centimeter.
c
c   The collimator is 95 w/o tungsten alloyed with 3.5 w/o nickel
c   and 1.5 w/o copper.
c
m13    plib=02p  elib=03e
      74000 -0.95
      28000 -0.035
      29000 -0.015
c
c   ------------------------
c   Aluminum Hardening Filter
c   ------------------------
c   Density of 2.7 grams per cubic centimeter.
c
```

```
m14    plib=02p  elib=03e
      13027  1
c
c   ----------------------
c   Steel Flattening Filter
c   ----------------------
c   Density of 7.9 grams per cubic centimeter.
c
c   The filter is iron (70 w/o) alloyed with 1 w/o silicon, 18 w/o
c   chromium, 2 w/o manganese and 9 w/o nickel.
c
m15    plib=02p  elib=03e
      26000 -0.70
      14000 -0.01
      24000 -0.18
      25000 -0.02
      28000 -0.09
c
c   -------------------
c   Lead Collimator Jaws
c   -------------------
c   Density of 11.35 grams per cubic centimeter.
c
m16    plib=02p  elib=03e
      82000  1
c
c   ----------------
c   Carbon Scatterer
c   ----------------
c   Density of 1.8 grams per cubic centimeter.
c
m17     plib=02p  elib=03e
       6000  1
c
c *******************
c  Source Description
c *******************
c
sdef  par 3            $ electrons
     pos 0 0 0         $ starting at the origin
     sur 201     rad=d1  $ distributed uniformly on the surface within a spot
     vec 0 0 -1  dir=1   $ perpendicularly incident
     erg d2            $ Gaussian in energy
c
c  Distribute particles uniformly within spot size of 0.05 cm.
```

```
si1    0.05
c
c  Gaussian in energy about 22.0 MeV.
#      si2    sp2
        l      d
       20.9  0.0054
       21.0  0.0141
       21.1  0.0335
       21.2  0.0725
       21.3  0.1433
       21.4  0.2589
       21.5  0.4268
       21.6  0.6426
       21.7  0.8833
       21.8  1.1087
       21.9  1.2707
       22.0  1.3298
       22.1  1.2707
       22.2  1.1087
       22.3  0.8833
       22.4  0.6426
       22.5  0.4268
       22.6  0.2589
       22.7  0.1433
       22.8  0.0725
       22.9  0.0335
       23.0  0.0141
       23.1  0.0054
c
c
c *****************
c  Physics Options
c *****************
c
c Transport electrons and photons
mode       e          p
c
c
c ***************
c  Print Options
c ***************
c
c Print everything
print
c
```

```
c
c *****************
c  Biasing Options
c *****************
c
wwp:e,p  5 3 5 0 0
wwe:e,p  1000
wwn1:e,p 0.2 56r -1 3r
elpt:e,p 0.1 60r
fcl:p    0 49r 1 0 9r
dxt:p    0.0  0.0  -100.0  0.71  0.71
     133.8  0.0  -100.0  0.26  0.26  1.0  1.E-13
c
c
c *********
c  Tallies
c *********
c
f102:p   521
e102     0.1 49i 23
c
f104:p   501
e104     0.1 49i 23
c
f204:p   602
e204     0.1 49i 0.6 23
c
c *****************
c  Runtime Options
c *****************
c
ctme 3260
```

REFERENCES CITED

Ahuja S D, Steward P G, Roy T S and Stessiner E D 1986 Estimated spectrum of a 4 MeV therapeutic beam Med. Phys. **13** 368-73

Ahnesjo A, Andreo P and Brahme A 1987 Calculation and application of point spread functions for treatment planning with high energy photon beams Acta Oncol. **26** 49-56

Ahnesjo A and Andreo P 1989 Determination of effective bremsstrahlung spectra and electron contamination for photon dose calculations Phys. Med. Biol. **34** 1451-64

4 Andreo P 1991 Monte Carlo techniques in medical radiation physics Phys. Med. Biol. **36** 861-920

Archer B R, Almond P R and Wagner L K 1985 Application of a Laplace transform pair model for spectral reconstruction Med. Phys. **9** 844-7

Archer B R and Wagner L K 1982 A Laplace transform pair model for high-energy x-ray spectral reconstruction Med. Phys. **12** 630-3

Baker C R, Ama'ee B and Spyrou N M 1995 Reconstruction of megavoltage photon spectra by attenuation analysis Phys. Med. Boil. **40** 529-42

Baker C R and Peck K K 1997 Reconstruction of 6 MV photon spectra from measured transmission including maximum energy estimation Phys. Med. Boil. **42** 2041-2051

13 Bentley R E, Jones J C and Lillicrap S C 1967 X-ray spectra from accelerators in the range 2 to 6 MeV Phys. Med. Biol. **12** 301-314

Boyer A and Mok E 1985 A photon dose distribution model employing convolution calculations Med. Phys. **12** 169-77

Boyer A and Mok E 1986 Calculation of photon dose distribution in an inhomogeneous medium using convolutions Med. Phys. **13** 503-9

10 Briesmeister J F (ed) 1997 MCNP-A General Monte Carlo N-particle Transport Code. Version 4B LA-12625-M (Los Alamos, NM: Los Alamos National Laboratory)

18 Chantler C T 1995 Theoretical form factor, attenuation, and scattering tabulation for Z = 1 - 92 from E = 1 - 10 eV to E = 0.4 - 1.0 MeV J. Phys. Chem. Ref. Data **24** 71-581

Dance D R 1987 A method for the reconstruction of diagnostic x-ray spectra from measurement of attenuation Phys. Med. Biol. **32** 1631-8

8 DeMarco J J, Solberg T D and Smathers J B 1998 A CT-based Monte Carlo simulation tool for dosimetry planning and analysis Med. Phys. **25** 1-11

15 Faddegon B A, Ross C K and Rogers D W O 1991 Angular distribution of bremsstrahlung from 15-MeV electrons incident on thick targets of Be, Al and Pb Med. Phys. **18** 727-739

9 Han K, Ballon D, Chui C and Mohan R 1987 Monte Carlo simulation of a cobalt-60 beam Med. Phys. **14** 414-419

Huang P, Kase K R and Bjarngard B E 1982 Simulation studies of 4 MV x-ray spectral reconstruction by numerical analysis of transmission data Med. Phys. **9** 695-702

Huang P, Kase K R and Bjarngard B E 1983 Reconstruction of 4-MV bremsstrahlung spectra from measured transmission data Med. Phys. **10** 778-85

17 Hubbell, J.H., Veigele, W.J., Briggs, E.A., Brown, R.T., Cromer, D.T., Howerton, R J 1975 Atomic form factors, incoherent scattering functions, and photon scattering cross sections J. Phys. Chem. Ref. Data **4** 471-538.

Krmar M, Slivka J, Bikit I, Veskovic, Conkic Jj, Bistrovic M and Rudic A 1993 A new method for the measurement of bremstrahlung spectra Phys. Med. Boil. **38** 533-44

16 Landy D Jand Anderson D W 1991 Measurement of accelerator bremsstrahlung spectra with a high-efficiency Ge detector Med. Phys. **18** 527-532

14 Levy L B, Waggener R G, McDavid W D and Payne W H 1974 Experimental and calculated bremsstrahlung spectra from a 25 MeV linear accelerator and a 19 MeV betatron Med. Phys. **1** 62-67

Levy L B, Waggener R G and Wright A E 1976 Measurement of primary bremsstrahlung spectrum from an 8 MeV linear accelerator Med. Phys. **3** 173-175

11 Lewis R D, Ryde S J S, Hancock D A and Evans C J 1999 An MCNP-based model of a linear accelerator x-ray beam Phys. Med. Biol. **44** 1219-1230

7 Liu H H, Mackie T R and McCullough E C 1997 A dual source photon beam model used in convolution/superposition dose calculations for clinical megavoltage x-ray beams Med. Phys. **24** 1960-74

6 Lovelock D M, Chui C S and Mohan R 1995 A Monte Carlo model of photon beams used in radiation therapy Med. Phys. **22** 1387-94

3 Mackie T R 1990 Applications of the Monte Carlo method in radiotherapy The Dosimetry of Ionizing Radiation vol 3, ed K R Kase, B Bjarngard and F H Attix (New York:Academic) pp541-620

Mackie T R, Bielajew A F, Rogers D W O and Battista J J 1988 Generation of photon energy deposition kernels using EGS Monte Carlo code Phys. Med. Biol. **33** 1-20

5 Mohan R, Chui C, and Lidofsky L 1986 Differential pencil beam dose computation model for photons Med. Phys. **13** 64-73

9 Mora G M, Maio A and Rogers D W O 1999 Monte Carlo simulation of a typical cobalt -60 therapy source Med. Phys. **26** 2494-2502

2 Morin R L (ed) 1988 "Monte Carlo Simulation in the Radiological Sciences" CRC Press

Nath R and Schulz R J 1976 Determination of high-energy x-ray spectra by photoactivation Med. Phys. **3** 133-41

12a Petti P L, M. S. Goodman, T. A. Gabriel, R. Mohan 1983a Investigation of buildup dose from electron contamination of clinical photon beams Med. Phys. **10** 18-24

12b Petti P L, M. S. Goodman, J. M. Sisterson, P. J. Biggs T. A. Gabriel, R. Mohan 1983b Sources of electron contamination for the Clinac-35 25 MV photon beams Med. Phys. **10** 856-861

Piermattei A, Arcovito G, Azario L, Bacci C, Bianciardi L and Giacco C 1990 A study of quality of bremsstrahlung spectra reconstructed from transmission measurements Med. Phys. **17** 227-33

1 Rogers D W O, Faddagon B A, Ding G X, Ma C M, Wei J and Mackie T R 1995 BEAM: A Monte Carlo code to simulate radiotherapy treatment units Med. Phys. **22** 503-524

Sam D, Bunney L R and Heater D C 1968 Gamma-ray pulse-height spectra: Formation of a response matrix for iterative unfolding Nucl. Instrum. Method **64** 148-156.

Sauer O and Neumann M 1990 Reconstruction of high-energy bremsstrahlung spectra by numerical analysis of depth-dose data Radiother. Oncol. **18** 39-47

Schiff L I 1951 Energy-angle distribution of thin-target bremsstrahlung Phys. Rev. **83** 252-3

19 Williamson J F, Deibel F C, and Morin R L 1984 The significance of electron binding correction s in Monte Carlo photon transport calculations Phys. Med. Biol. **29** 1063-

Zhu Y and Boyer A 1990 X-ray dose computation in heterogeneous media using 3-dimentional FFT convolution Phys. Med. Biol. **35** 351-68

BIOGRAPHICAL SKETCH

Texin Li was born in 1967 in Hunan, China. He graduated from Shaanxi Normal University with a Bachelor of Science degree in physics in 1989. Enrolled in the graduate program in 1989 in the physics department at Shaanxi Normal University, he spent more than a year (from 1991 to 1992) as a visiting research fellow at the Institute of Physics, Chinese Academy of Sciences. He got his Master of Science degree in laser physics in 1992. After graduation, Mr. Li worked as a physics instructor in the physics department of Shaanxi Normal University till 1996 when he was admitted to the Ph.D. program in the Department of Nuclear and Radiological Engineering at the University of Florida.

I certify that I have read this study and that in my opinion it conforms to acceptable standards of scholarly presentation and is fully adequate, in scope and quality, as a dissertation for the degree of Doctor of Philosophy.

Samim Anghaie, Chairman
Professor of Nuclear and
Radiological Engineering

I certify that I have read this study and that in my opinion it conforms to acceptable standards of scholarly presentation and is fully adequate, in scope and quality, as a dissertation for the degree of Doctor of Philosophy.

Edward Dugan
Associate Professor of Nuclear and
Radiological Engineering

I certify that I have read this study and that in my opinion it conforms to acceptable standards of scholarly presentation and is fully adequate, in scope and quality, as a dissertation for the degree of Doctor of Philosophy.

Jatinder R Palta

Jatinder Palta
Professor of Nuclear and
Radiological Engineering

I certify that I have read this study and that in my opinion it conforms to acceptable standards of scholarly presentation and is fully adequate, in scope and quality, as a dissertation for the degree of Doctor of Philosophy.

Chihray Liu
Associate Professor of Nuclear and
Radiological Engineering

I certify that I have read this study and that in my opinion it conforms to acceptable standards of scholarly presentation and is fully adequate, in scope and quality, as a dissertation for the degree of Doctor of Philosophy.

Siyong Kim
Assistant Professor of Radiation
Oncology

I certify that I have read this study and that in my opinion it conforms to acceptable standards of scholarly presentation and is fully adequate, in scope and quality, as a dissertation for the degree of Doctor of Philosophy.

James Klausner

James Klausner
Professor of Mechanical
Engineering

I certify that I have read this study and that in my opinion it conforms to acceptable standards of scholarly presentation and is fully adequate, in scope and quality, as a dissertation for the degree of Doctor of Philosophy.

Robert J Han

Robert J. Hanrahan
Professor of Chemistry

This dissertation was submitted to the Graduate Faculty of the College of Engineering and to the Graduate School and was accepted as partial fulfillment of the requirements for the degree of Doctor of Philosophy.

December 2000

M. Jack Ohanian
Interim Dean, College of
Engineering

Winfred M. Phillips
Dean, Graduate School
Vice President